

1 This manuscript has been submitted for publication in the Journal of
2 Geophysical Research: Solid Earth. The article has not yet been peer re-
3 viewed and subsequent versions of this manuscript may be different. If ac-
4 cepted, the final version of this manuscript will be available via the ‘Peer-
5 reviewed Publication DOI’ link on the right-hand side of this webpage. Please
6 feel free to contact the corresponding author, we welcome feedback

7 **Parsimonious velocity inversion applied to the Los**
8 **Angeles Basin, CA**

9 **Jack B. Muir^{1,2}, Robert W. Clayton¹, Victor C. Tsai³, and Quentin Brissaud⁴**

10 ¹Seismological Laboratory, Division of Geological and Planetary Sciences, California Institute of
11 Technology, Pasadena, CA, USA

12 ²Research School of Earth Sciences, Australian National University, Acton, ACT, Australia

13 ³Department of Earth, Environmental and Planetary Sciences, Brown University, Providence, RI, USA

14 ⁴NORSAR, Oslo, Norway

15 **Key Points:**

- 16 • We generate a new velocity model of the northeastern Los Angeles Basin
17 using data from the Community Seismic Network
18 • Using a level-set framework, we parsimoniously balance the existing
19 Community Velocity Models with new data constraints
20 • The new model indicates a steeper and deeper basin underneath down-
21 town Los Angeles, significantly amplifying 4–6 s Love waves

Corresponding author: Jack B. Muir, jmuir@caltech.edu

22 **Abstract**

23 The proliferation of dense arrays promises to improve our ability to im-
 24 age geological structures at the scales necessary for accurate assessment of
 25 seismic hazard. However, combining the resulting local high-resolution to-
 26 mography with existing regional models presents an ongoing challenge. We
 27 developed a framework based on the level-set method that infers where lo-
 28 cal data provide meaningful constraints beyond those found in regional mod-
 29 els - e.g. the Community Velocity Models (CVMs) of southern California.
 30 This technique defines a volume within which updates are made to a ref-
 31 erence CVM, with the boundary of the volume being part of the inversion
 32 rather than explicitly defined. By penalizing the complexity of the bound-
 33 ary, a minimal update that sufficiently explains the data is achieved.

34 To test this framework, we use data from the Community Seismic Net-
 35 work, a dense permanent urban deployment. We inverted Love wave dis-
 36 persion and amplification data, from the Mw 6.4 and 7.1 2019 Ridgecrest
 37 earthquakes. We invert for an update to CVM-S4.26 using the Tikhonov
 38 Ensemble Sampling scheme, a highly efficient derivative-free approximate
 39 Bayesian method. We find the data are best explained by a deepening of
 40 the Los Angeles Basin with its deepest part south of downtown Los Ange-
 41 les, along with a steeper northeastern basin wall. This result offers new progress
 42 towards the parsimonious incorporation of detailed local basin models within
 43 regional reference models utilizing an objective framework and highlights
 44 the importance of accurate basin models when accounting for the amplifi-
 45 cation of surface waves in the high-rise building response band.

46 **1 Introduction**

47 The Los Angeles (LA) Basin is a deep sedimentary structure whose evo-
 48 lution can be roughly characterized by an initial subsidence and extensional
 49 phase during the establishment of the North America - Pacific plate bound-
 50 ary associated with the opening of the Gulf of California and the rotation
 51 of the Transverse Ranges in the Miocene. This was followed by a period of
 52 transpression (Ingersoll & Rumelhart, 1999), and the generation of a sub-
 53 stantial network of thrust faults within the basin (Wright, 1991). In its cur-
 54 rent state, the basin contains both active strike-slip faults (e.g. the Newport-
 55 Inglewood fault, Whittier-Elsinore fault) and an imbricated stack of blind
 56 thrust faults (e.g. the Elysian Park faults, Puente Hills thrust), all of which
 57 accommodate the transpressional motion of the basin. These faults contribute
 58 to local seismic hazard both by providing source surfaces for earthquakes
 59 and by controlling local path effects by shaping the basin geometry (Plesch
 60 et al., 2007). The evolutionary history of the LA basin, with ample oppor-
 61 tunity to produce and bury organic material during extension followed by
 62 the establishment of stratigraphic traps during compression, has allowed
 63 LA to be a leading producer of oil in the United States (US), helping to fuel
 64 a large rise in population during the mid-20th century. Development took
 65 place predominantly on the soft sediments of the main LA, San Fernando,

66 San Gabriel and San Bernardino basins. As a consequence, LA is both one
67 of the largest and most economically important cities in the US, while also
68 being one of the most exposed to significant earthquake hazard due to the
69 complex fabric of active faults and ground-motion amplifying sedimentary
70 structures associated with the geology that has allowed its preeminence.

71 Seismic hazard within the basin is controlled by the locations and po-
72 tential for slip on the multiple local and regional faults of southern Califor-
73 nia, combined with the significant amplifying effect of the basin on ground
74 motions. The importance of path effects, such as wavefield focusing, mul-
75 tipathing, and basin amplification, on LA basin ground motions has moti-
76 vated extensive development of seismic velocity models. The ultimate goal
77 of these models is to produce accurate synthetic waveforms at frequency ranges
78 relevant to infrastructure and building codes within the basin. Early efforts
79 focused on creating rule-based models of southern California (Magistrale
80 et al., 1996, 2000) using empirically derived velocity laws (Faust, 1951) in
81 combination with inferred geological structure obtained by correlating sur-
82 face outcrops, borehole profiles and potential methods (Wright, 1991). Since
83 these initial efforts, regional scale models of southern California have assim-
84 ilated ever greater quantities of seismic data, including seismic reflection pro-
85 files, receiver functions, and earthquake source locations and mechanisms.
86 This increase in the amount of data has led to better demarcated bound-
87 aries, including faults (Magistrale et al., 2000; Plesch et al., 2007), and al-
88 lowed for more lateral variation of within basin velocity structures by us-
89 ing geostatistical methods to tie together disparate seismic data (Süss & Shaw,
90 2003; Shaw et al., 2015). Continued development of seismic velocity mod-
91 els of southern California has resulted in two widely used reference Com-
92 munity Velocity Models (CVMs), CVM-S4.26 (Lee et al. (2014), CVM-S here-
93 after) and CVM-H 15.1.0 (Shaw et al. (2015), CVM-H hereafter), that have
94 incorporated waveform based seismic tomography to further refine the mod-
95 els. CVM-S and CVM-H broadly agree in the positions, average velocity pro-
96 file, and geometry of the major basins of southern California, however in
97 detail they are quite different, with CVM-H containing more explicit geo-
98 logical information. Figure 1 shows a characteristic cross-section of the LA
99 basin for both models, running from Catalina Island, across the Inner Bor-
100 derland to Palos Verdes, then through the main LA basin, San Gabriel basin
101 and through the Transverse Ranges to the high desert. This profile makes
102 evident the considerably higher detail present in the CVM-H model due to
103 its construction including explicit geological features (notably including an
104 Inner Borderland basin not present in CVM-S, as seen to the left of profile
105 A–B in Figure 1), as well as its significant artefacts associated with chang-
106 ing lateral resolution, as evident in profile marks R1 and R2. In contrast,
107 CVM-S is significantly smoother than CVM-H due to its reliance on waveform-
108 tomography during the final stages of construction, although several sharp
109 resolution based artefacts are also evident, such as the jagged edges of the
110 San Gabriel basin. Many features of the seismic wavefield within the LA
111 basin, such as phase arrival times and P-to-S amplitude ratios, are captured
112 for local events at frequencies of up to 0.2 Hz (Taborda et al., 2016; Lai et

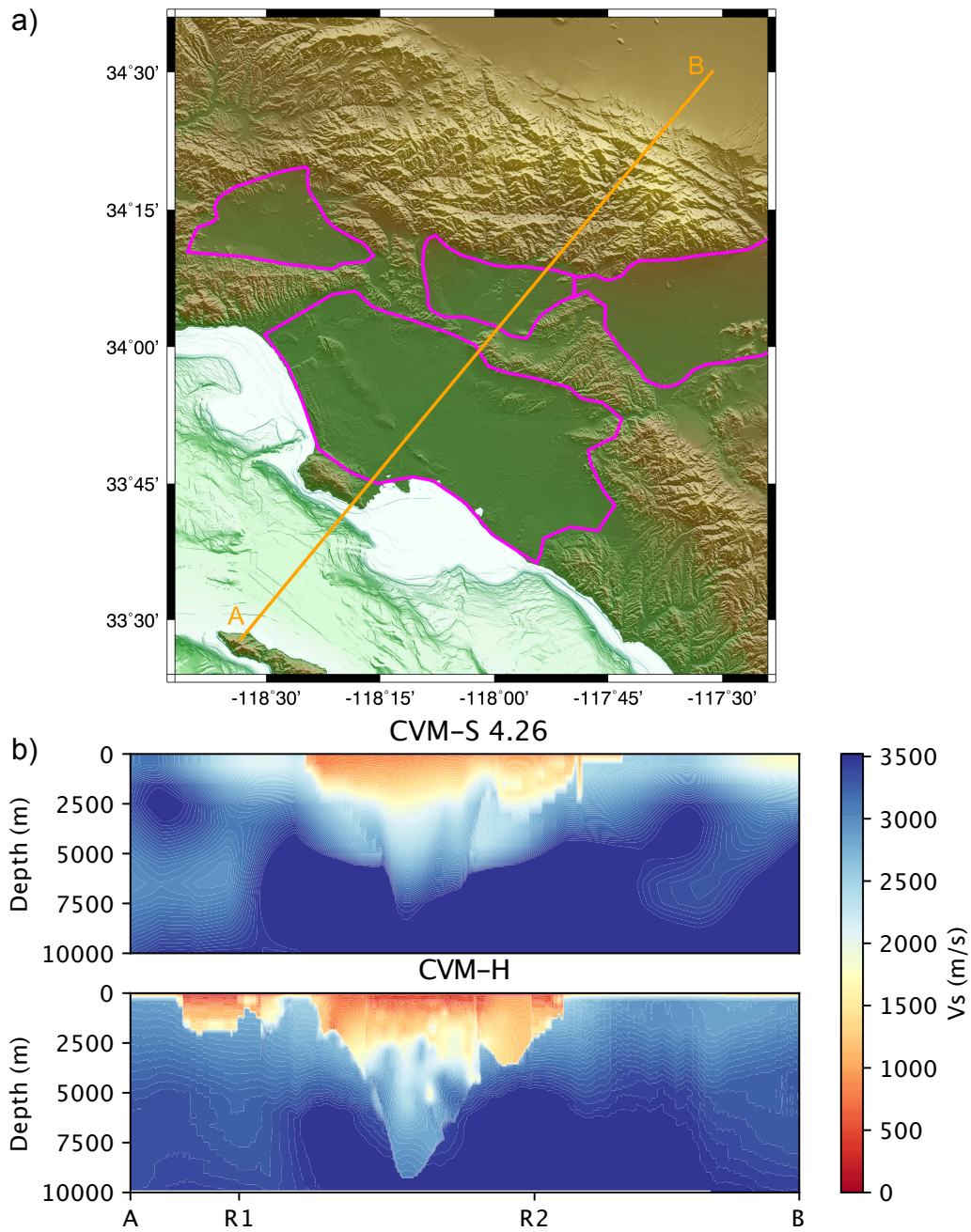


Figure 1.

a) Shaded elevation model of southern California showing the outline of the major basins (defined by slope-break analysis) in purple and the transect A-B used for profiles shown in orange. b) Characteristic profiles through the Los Angeles basin for the CVM-S and CVM-H models. Abrupt lateral changes in resolution at positions R1 and R2 are seen in the CVM-H model.

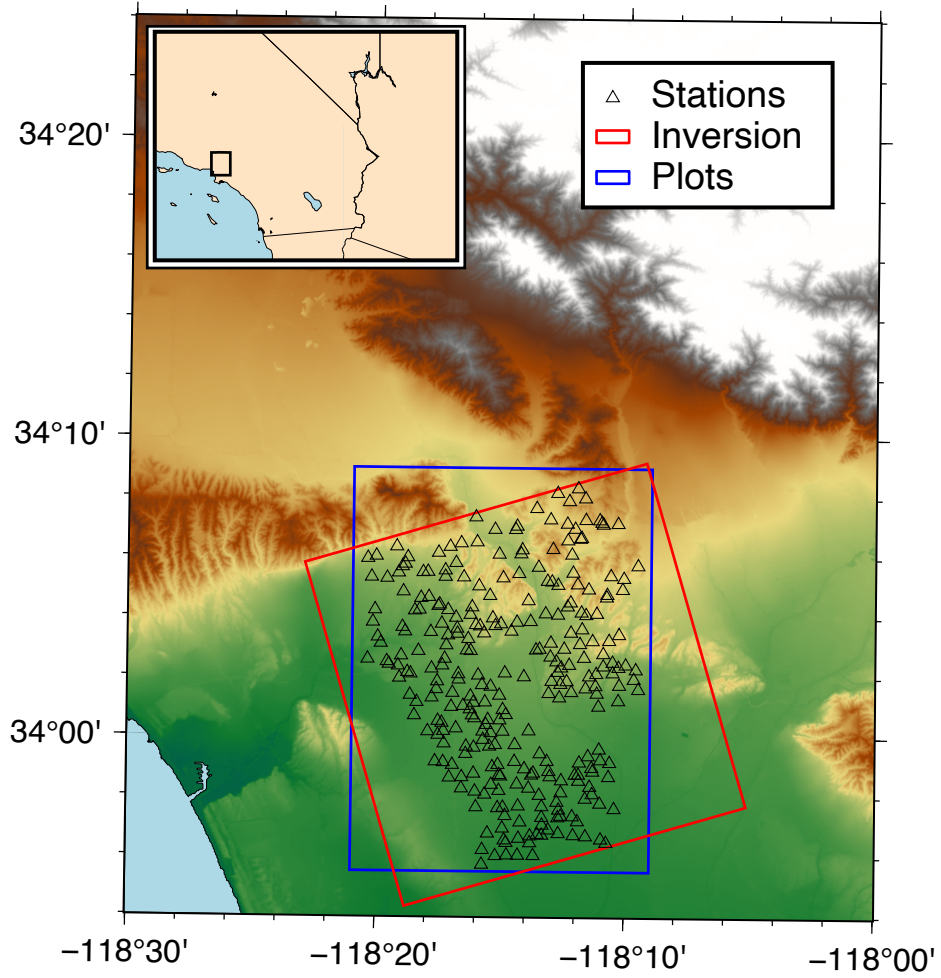


Figure 2. Map of the study region, showing the locations of the CSN stations as open triangles, the boundary of the square inversion region in red, and the boundary of the analysis plots in blue.

113 al., 2020). However, excitations of the basin from the recent large regional
114 Ridgecrest earthquake sequence in July 2019 have illustrated that ground
115 motion amplification predictions from finite-difference wave propagation through
116 the SCEC CVM-H and CVM-S models do not accurately predict the ob-
117 servations in the 0.1-1 Hz range that is relevant for tall buildings within down-
118 town LA (Filippitzis et al., 2021), warranting continued close study of the
119 LA basin velocity model.

120 Seismic tomography offers the best opportunity for full spatial cover-
121 age of the basin at high resolution, especially when dense seismic arrays are
122 utilized. In the southern and central parts of the basin, the deployment of
123 high-density temporary seismic arrays using 10 Hz corner-frequency geo-
124 phone nodes by the petroleum industry has enabled considerable exploration
125 of the shallow structure of the basin using ambient-noise derived observables,
126 such as Rayleigh-wave phase velocities, Rayleigh-wave amplifications, and
127 body-wave travel times (e.g. Lin et al. (2013); Bowden et al. (2015); Castel-
128 lanos et al. (2020); Jia & Clayton (2021)). However, similarly dense indus-
129 try deployments have not to date taken place in the northern part of the
130 basin, which encompasses the downtown LA region, with buildings that are
131 highly susceptible to resonant coupling to the basin. The permanent broad-
132 band southern California Seismic Network (SCSN), while providing a long
133 time series of excellent quality observations, has already been incorporated
134 into the CVM reference models and does not provide the spatial resolution
135 required for the next generation of basin models. A potential alternative
136 data source is the Community Seismic Network (CSN, Clayton et al. (2012,
137 2020)), a permanent network of three-component micro-electromechanical
138 system (MEMS) accelerometers, designed to provide real-time strong-ground-
139 motion telemetry in the event of local earthquakes within the LA basin. The
140 CSN instruments have been designed for inexpensive construction, utiliz-
141 ing off-the-shelf components, and have a maximum observable acceleration
142 of $\pm 2g$, in order to fulfil their primary goal of strong-ground-motion mon-
143 itoring. As a result, the instrument noise floor is above the amplitude of ground
144 motions produced by smaller regional earthquakes, and is also above the am-
145 bient seismic noise level. This unfortunately precludes the use of ambient-
146 noise cross-correlation methods on CSN data as these methods rely on co-
147 herent low-level energy propagation between sensors. However, both the Mw
148 6.4 and Mw 7.1 2019 Ridgecrest, California earthquakes produced high qual-
149 ity records across the array, allowing for detailed analysis of ground ampli-
150 fication within the basin (Kohler et al., 2020; Filippitzis et al., 2021). The
151 coherent surface-wave energy from these two events, recorded on the CSN,
152 offers a unique opportunity to construct a high-resolution local tomographic
153 model of the northeastern edge of the LA basin. In this study, we use the
154 phase velocity and relative amplitudes of Love waves from both events, along
155 with a 3D surface-wave tomography method based on the level-set method
156 of Muir & Tsai (2020), to create such a model. The level-set framework ex-
157 tends traditional tomography by allowing for implicitly defined discontin-
158 uous interfaces within a velocity model. For instance, Muir & Tsai (2020)
159 used the level-set method to image the damage zone of the San Andreas Fault

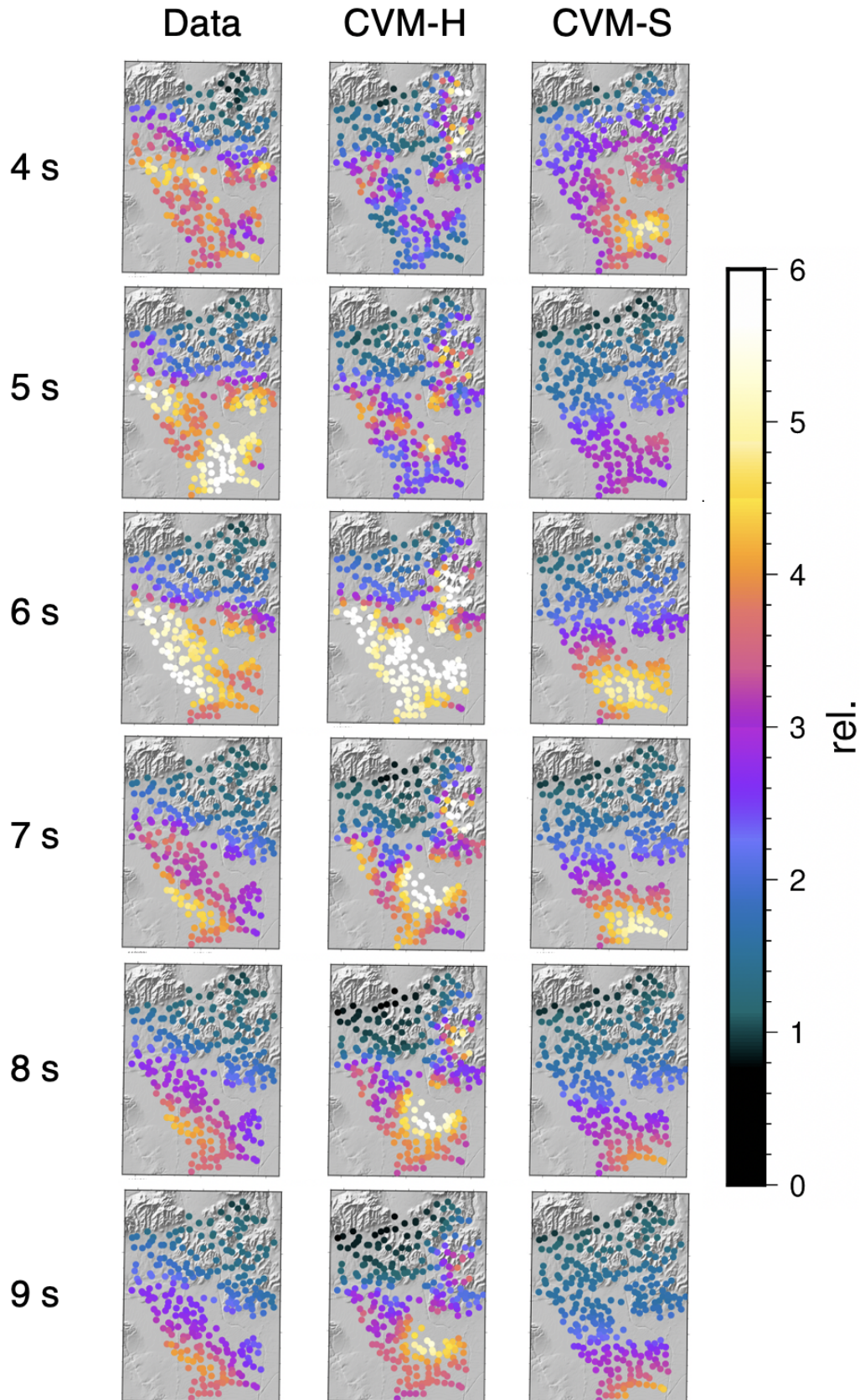


Figure 3.

Relative amplification of the maximum amplitude of 3 component pseudo-spectral accelerations (PSA) in the range of 4–9 s from the Mw 7.1 July 5 2019 Ridgecrest earthquake as recorded on the Community Seismic Network (CSN), and as simulated using the Graves and Pitarka rupture generator (Pitarka et al., 2019) and a 3D finite-difference waveform solver for both the CVM-H and CVM-S models (Graves, 1996).

160 at Carrizo Plains using a three-layer model, whereas Tso et al. (2021) pre-
 161 sented several applications of the level-set method for developing interpretable
 162 block models of electrical resistivity. The ability to handle implicitly defined
 163 discontinuities significantly extends traditional tomographic methods, which
 164 usually require restrictive and unphysical regularization schemes to be well-
 165 posed. We use the level-set method to define a basin volume within which
 166 we update a local model — this method allows us to only alter the refer-
 167 ence CVM model where we have sufficient data constraints to warrant an
 168 update. We take a quasi-Bayesian approach to local updating in which the
 169 reference CVM becomes the *a priori* favored model within the local update.
 170 The Love wave data set then updates the CVM prior into an approximate
 171 posterior model which includes the influence of both the new data and the
 172 data that went into the CVM via its expression in the CVM model. At a
 173 global scale, a similar scheme of local quasi-Bayesian model refinement has
 174 been proposed by Fichtner et al. (2018), and within the SCEC CVM frame-
 175 work Ajala & Persaud (2021) have proposed a means of blending local up-
 176 dates into existing regional models — this work differentiates itself by its
 177 data-driven choice of model updating region, consistent with estimated data
 178 uncertainty. Integration of local models within the SCEC CVM framework
 179 will become an important part of hazard modelling within Southern Cal-
 180 ifornia as high-density arrays allow access to the fine scale detail of path ef-
 181 fects. The framework presented in this study represents a parsimonious way
 182 to achieve this integration.

183 2 Data Collection

184 2.1 Preprocessing

185 The data for this study were obtained from the HN accelerometer chan-
 186 nels of the Los Angeles Unified School District (LAUSD) subarray of the
 187 Community Seismic Network (CSN, Clayton et al. (2012, 2020)), consist-
 188 ing of 200 s time series after the Mw 6.4 and Mw 7.1 Ridgecrest earthquakes’
 189 origin times and recorded at 50 samples/sec. The network is deployed within
 190 school buildings in the City of Los Angeles, and at the time of the Ridge-
 191 crest earthquakes consisted of 300 stations spaced approximately 0.5 km apart.
 192 We used the components of the CSN located within the northeast LA basin,
 193 which is the densest part of the array. The study area, including the loca-
 194 tions of the stations, is shown in Figure 2. Various display of the Ridgecrest
 195 earthquake data are shown in Filippitzis et al. (2021), along with a com-
 196 parison of the data and predicted ground motions by several methods. For
 197 our study, data were first detrended, rotated into the *ZRT* frame, decimated
 198 to 5 Hz and then detrended once more. Pseudo-spectral accelerations (PSA)
 199 were then calculated for both the real data and synthetic 3D finite-difference
 200 simulations following the Graves and Pitarka method (Graves & Pitarka,
 201 2010; Pitarka et al., 2019) for both the CVM-H and CVM-S models by con-
 202 volving the records with a 5% damped harmonic oscillator, with the results
 203 for 4–9 s period shown in Figure 3. A record section of the high-frequency
 204 strong-ground-motion-accelerometer transverse (HNT) channel showing strong

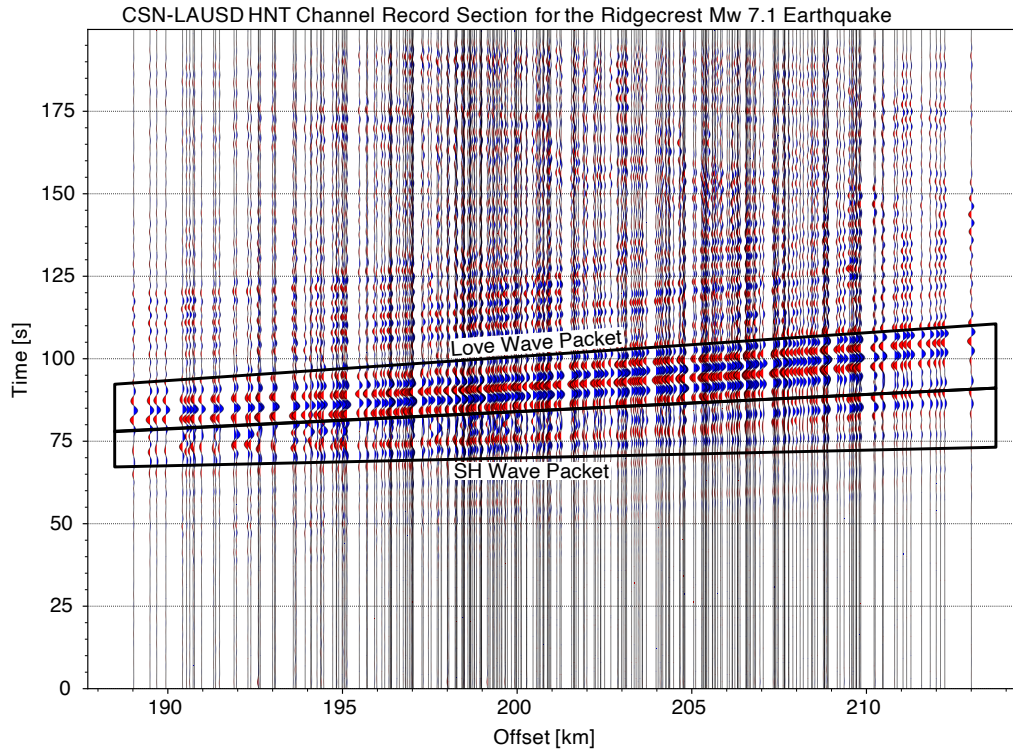


Figure 4.

Record Section of the Mw 7.1 Ridgecrest earthquake as recorded on the HNT channel of the CSN-LAUSD array, zero-phase bandpass filtered between 4–10 s. Two main phases are clearly identifiable, with the first arriving phase exhibiting little delay due to the basin at longer offsets, which we infer to be the primary SH arrival. A second, stronger phase, which is delayed by the basin at longer offsets, we infer to be the fundamental Love mode.

205 SH polarized phases corresponding to the fundamental Love mode is shown
 206 in Figure 4.

207 **2.2 Love Group Arrival Time and Amplitude Picks**

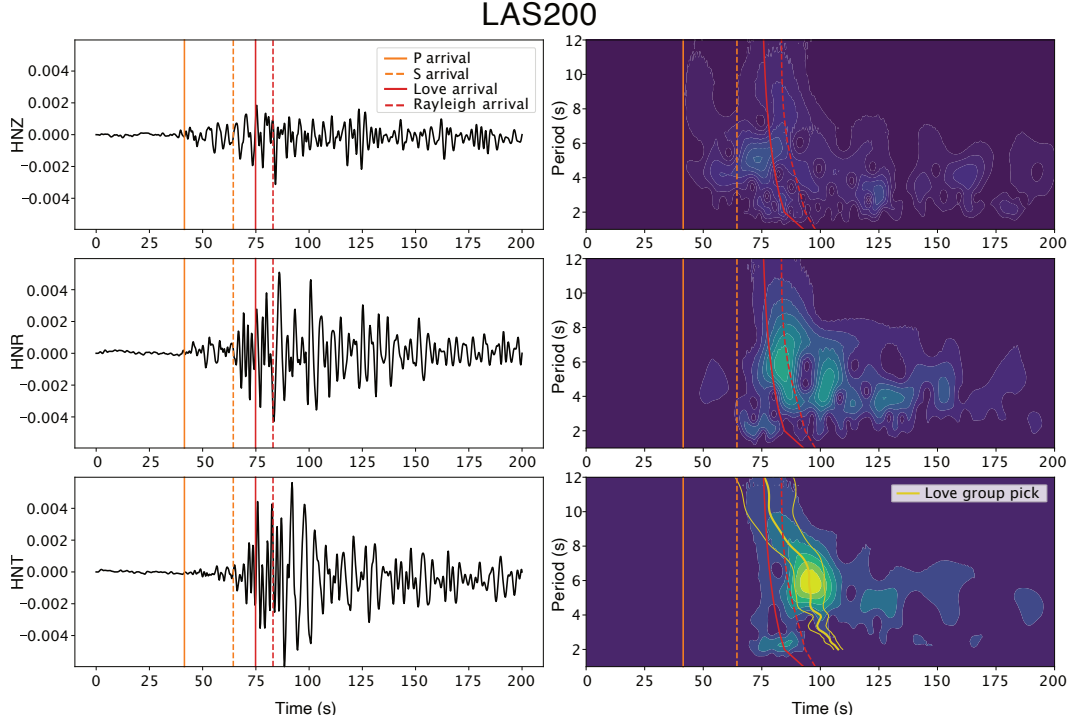


Figure 5.

HN waveforms and corresponding continuous-wavelet transform spectrograms for the LAUSD CSN station LAS200 from the July 5 2019 Ridgecrest Mw 7.1 earthquake. The solid and dashed orange lines show the theoretical arrival times of the P and S waves through the laterally averaged CVM-H model from the hypocentral location to LAS200, and the solid and dashed red lines show the theoretical group arrivals for Love and Rayleigh waves, respectively. All theoretical travel times are offset from the event origin time by 10 s, which is the approximate peak of the USGS moment rate function. The yellow lines show the center and $\pm 1\sigma$ width of the fitted Gaussian functions to the envelope of the tangential component. The center of these Gaussian functions act as group delay picks for defining the cross-correlation window used for two-station phase delay measurements shown in Figure 6.

208 To make group arrival picks, raw waveforms were first narrow-band fil-
 209 tered at period P using a zero-phase Butterworth bandpass filter with cor-
 210 ners at $1/P \pm 1/(\sqrt{20}P)$ and then cosine tapered over the first 20 s of the
 211 time series to suppress edge effects. The maximum of the T component en-
 212 velopes at a central period $P = 12.5$ s were set as the first preliminary group
 213 arrival pick. The 12.5 s filtered waveform envelopes were then again cosine-
 214 tapered with a $6P$ taper window with $1P$ edges about this preliminary pick.

215 We then fit a Gaussian function to the waveform envelope, with the center
 216 of the Gaussian being used as the finalized group arrival pick at 12.5 s
 217 and the amplitude of the Gaussian being recorded as the Love wave ampli-
 218 tude. Starting with the parameters of the 12.5 s Gaussian as initial values,
 219 we then proceeded to work down in 0.25 s increments on the narrowband
 220 filtered waveform envelopes, to a minimum period of 2 s. We tapered with
 221 the $6P$ width cosine around the Gaussian center of the previous period. We
 222 then fit a new Gaussian to the shorter-period waveform, initialized using
 223 the previous period’s Gaussian fit. This method tracks the Love-wave group
 224 arrival from long periods, where it is clearly identifiable as the strongest fea-
 225 ture, to shorter periods where other features are present. A characteristic
 226 example of the group picks is shown in Figure 5.

227 We took the logarithms of the fitted Gaussian amplitudes and normal-
 228 ized them relative to the mean log at each period to create the amplitude
 229 data set. The relatively narrow aperture of the CSN array compared to the
 230 distance to the source meant that the geometry was not favorable for tra-
 231 ditional tomographic methods. We therefore employed eikonal tomography
 232 (Lin et al., 2009, 2014) to calculate surface-wave dispersion curves, which
 233 has the additional advantage of naturally handling the curving wavefronts
 234 recorded on the CSN, caused by refraction across the basin boundary. Al-
 235 though recent studies (Qiu et al., 2019) have attempted to utilize group ar-
 236 rival times for eikonal tomography of group velocity, there is significant noise
 237 associated with the group arrival peak. Furthermore, there are strict con-
 238 ditions on the approximations necessary for using eikonal tomography on
 239 group delay times that may not be met when the surface-wave arrival ex-
 240 periences refraction across a basin boundary (Qiu et al., 2019). As such, we
 241 did not attempt to utilize group velocity c_g in this study, but rather used
 242 the group times as a guide for two-station cross-correlation phase delay times
 243 as discussed below.

244 **2.3 Eikonal Tomography from Two-Station Cross-Correlation** 245 **Phase-Delay Times**

246 We employ eikonal tomography (Lin et al., 2009) to obtain phase ve-
 247 locity estimates within the densely spaced CSN array. Eikonal tomography
 248 obtains phase velocity c directly from the gradient of the phase delay field:
 249 $|\nabla\tau| \approx 1/c$. Eikonal tomography has two principle requirements. Firstly,
 250 there must be a clearly identifiable phase delay field τ (i.e. there is no sig-
 251 nificant multipathing), a requirement which is met for Love waves in the pe-
 252 riod range of this study. Secondly, eikonal tomography is derived from an
 253 approximation of the transport equation $1/c^2 = |\nabla\tau|^2 - \nabla^2 A/A\omega^2$, where
 254 ignoring the amplitude correction is typically taken to be valid for veloc-
 255 ity models that are sufficiently laterally smooth that the Laplacian of the
 256 amplitude is small. Waves propagating from the Ridgecrest earthquake se-
 257 quence strike the northeastern edge of the Los Angeles Basin nearly per-
 258 pendicularly, so any effect of the basin edge on the Laplacian term is lim-
 259 ited in extent within the LAUSD-CSN array. It is possible to utilize the full

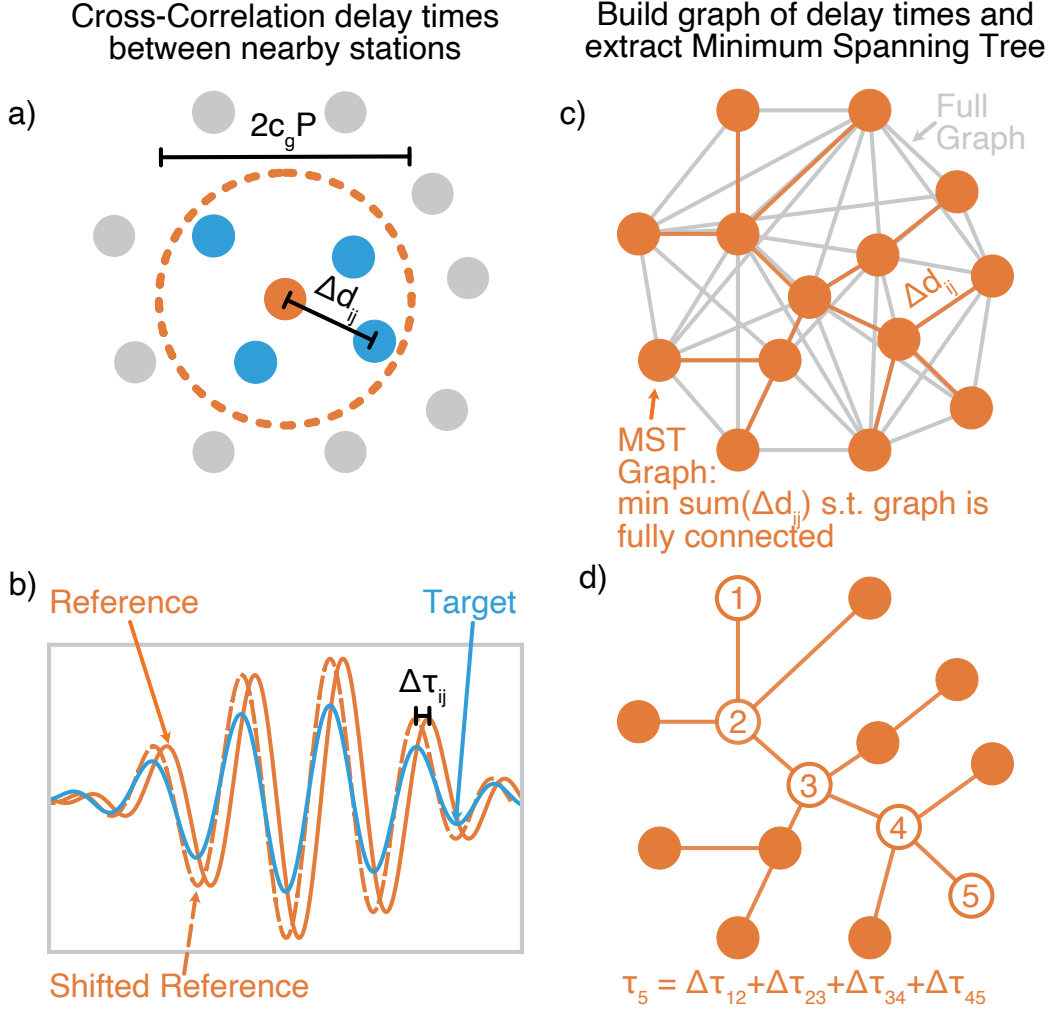


Figure 6.

Outline of steps used to construct the phase delay field τ from narrowband filtered records. In the first two steps, the phase delays between all nearby stations are computed. In a), we draw a circle of radius $r_{ij} < \max(c_g P, 0.5P)$ and compute the phase delay for maximum cross-correlation, $\Delta\tau_{ij}$, as shown in b). Only nearby stations are used to suppress cycle skipping. In the second phase, we extract the minimum spanning tree (MST) from the graph of collected phase delay times, as shown in c). The MST is a sub-graph that minimizes the total edge lengths (i.e. Δd_{ij}) such that the graph is still fully connected. Finally, in d) we traverse the MST from the northernmost station, summing $\delta\tau_{ij}$ along the edges to get the τ , a minimum-relative-phase-delay surface concordant with the recorded relative phase delays between individual station pairs.

260 transport equation for determining phase velocity, which is called Helmholtz
 261 tomography and may provide improved accuracy if the Laplacian of the am-
 262 plitude can be accurately calculated (Lin & Ritzwoller, 2011). For this data
 263 set, comparisons between Helmholtz tomography and eikonal tomography
 264 show agreement across the basin transition where we would expect the am-
 265 plitude correction to be strongest, which implies that eikonal tomography
 266 is sufficient to capture the correct phase velocity in the center of the array.
 267 Spurious values of the Helmholtz tomography solutions occur on the edges
 268 of the array due to the difficulty of obtaining accurate values of the Lapla-
 269 cian of the amplitude. Consequently, we limit our data analysis to the phase
 270 velocities derived from the eikonal equation as its assumptions appear to
 271 be satisfactorily realized and the Helmholtz tomography corrections are not
 272 sufficiently robust given our data.

273 In order to obtain the phase delay field τ at period P (relative to the
 274 northernmost station of the array), we first narrowband filter wavepackets
 275 at central period P . We then taper the waveform around the group arrival
 276 time using a cosine taper with a flat window of width $4P$ and edges of width
 277 P . We then calculate the cross-correlation time delay $\Delta\tau_{ij}$ between each pair
 278 of stations i and j within a circle of radius $r_{ij} < \max(c_g P, c_{min} P)$ with a
 279 cutoff velocity $c_{min} = 0.5\text{km/s}$. The distance limit reduces the impact of
 280 potential cycle skipping on the phase delay observations, whereas the nar-
 281 rower taper width compared to the group picks also helps to stabilize the
 282 cross-correlation calculations. This process is illustrated in Figure 6 a) and
 283 b). The relative delays $\Delta\tau_{ij}$ form a graph with stations acting as nodes and
 284 the delays acting as edge weights. Similarly, the distances between stations
 285 Δd_{ij} also form a graph. Appealing to Fermat’s principle of least travel time,
 286 we extract the minimum spanning tree (MST) of the station distance graph,
 287 and then use the geometry of the MST to find an approximate minimum
 288 travel time surface. The MST is a unique sub-graph that connects all nodes
 289 (stations) with minimum edge weights (distances), with a schematic of this
 290 subgraph shown in Figure 6 c). Summing phase delays $\Delta\tau_{ij}$ along MST edges
 291 from the northernmost station gives a minimum relative travel time surface
 292 that is concordant with the observed phase delay data, as shown in Figure
 293 6 d). We also tested MSTs extracted from both the graph of normalized cross-
 294 correlation values, as well as the graph of phase delays themselves, but found
 295 that the MST based on distance weighting gave the best performance in the
 296 final phase velocity maps. We then smooth the travel-time surface at each
 297 period by first fitting a high-tension cubic spline to the data, removing all
 298 outlying data points for which the fit residual at that point was greater than
 299 one standard deviation of all collected residuals, and then refitting the spline
 300 to the remaining data. This outlier removal cleans the phase delay dataset
 301 of any remaining cycle-skipped measurements. This smoothed surface τ is
 302 then used to calculate phase velocity c at period p using the eikonal equa-
 303 tion $|\nabla\tau| = 1/c$.

304

2.4 Estimating Measurement Uncertainty

305

306

307

308

309

310

311

312

313

314

315

316

317

318

319

320

321

The only available earthquakes that have produced sufficiently strong ground motions to record at least one octave of frequencies of Love waves are the Mw 6.4 and Mw 7.1 Ridgecrest events. Two events are insufficient to obtain useful statistical estimates of measurement uncertainty using only data recorded at individual stations. However, given that the surface-wave measurements have a finite area of sensitivity that overlaps substantially between neighbouring stations, we can approximate the measurement uncertainty at a point by including all data within the sensitivity area. To calculate this, we bin data statistics over subarrays of radius $\lambda/4$ to obtain an estimate of the measurement uncertainty, where λ is the fundamental Love wavelength at the period of measurement and the station of interest. At station i , we calculate the mean of the relative log amplitude $\tilde{a}^i = (a_{6.4}^i + a_{7.1}^i)/2$ and phase velocity $\tilde{c}^i = (c_{6.4}^i + c_{7.1}^i)/2$ where $a_{6.4}$ and $c_{6.4}$ are the amplitude and phase velocities for the Mw 6.4 earthquake, respectively, and likewise $a_{7.1}$ and $c_{7.1}$ are the amplitude and phase velocity for the Mw 7.1 earthquake. We then estimate the 1σ uncertainty in the mean by averaging over the data variance at nearby stations:

322

$$\sigma_a^i = \sqrt{\sum_{j \in d_{ij} \leq \lambda/4} (a_{6.4}^j - \tilde{a}^j)^2 + (a_{7.1}^j - \tilde{a}^j)^2} / \sqrt{2} \quad (1)$$

323

$$\sigma_c^i = \sqrt{\sum_{j \in d_{ij} \leq \lambda/4} (c_{6.4}^j - \tilde{c}^j)^2 + (c_{7.1}^j - \tilde{c}^j)^2} / \sqrt{2} \quad (2)$$

324

325

326

327

328

329

where d_{ij} is the distance between stations i and j . The uncertainty correlation matrix P_{ij} is modeled using a squared-exponential covariance function with characteristic length scale equal to one quarter of the average Love wavelength at predicted at stations i and j , which accounts for spatially correlated uncertainty, with the addition of a diagonal term to account for uncorrelated uncertainties

330

$$P_{ij} = \delta_{ij} + \exp(-8d_{ij}^2/(\lambda_i + \lambda_j)^2), \quad (3)$$

331

332

333

334

335

336

337

338

339

where δ_{ij} is the Kronecker delta. For each period the empirical uncertainty covariance matrices are therefore given by $\Gamma_c = \sigma_c P \sigma_c^T$ and $\Gamma_a = \sigma_a P \sigma_a^T$ where σ_c is the collected vector of individual station phase-velocity uncertainty measurements across all periods, and σ_a is likewise the vector of amplitude uncertainty measurements. Future work on uncertainty modelling could account for a variable scaling between the diagonal and non-diagonal terms in P , and model the correlations between measurements at neighboring periods; however for reasons of computational expediency we do not develop these analyses here.

340

3 Inversion Methodology

341

3.1 Model Parameterization

342

343

344

Having obtained measurements \tilde{c} and \tilde{a} and associated data uncertainty matrices Γ_c and Γ_a for phase velocity and log-relative amplification within the CSN, we are now in a position to model them and invert for a local basin

345 update. We seek to obtain a parsimonious local update that balances the
 346 constraints of new, densely recorded data, with the already well developed
 347 models presented in the SCEC CVMs. Ideally, we would perform a fully Bayesian
 348 inversion taking a CVM as a prior model; however as robust model uncertain-
 349 tainties for the CVMs are not available, this approach would be highly de-
 350 pendent on subjective estimates for setting the prior, and would further-
 351 more be extremely computationally expensive for the nonlinear forward mod-
 352 els required to predict our recorded data. Instead, we recognize that the sen-
 353 sitivity of our data is highly contained within the basin itself, given the char-
 354 acteristic phase velocities c and periods p of our study and the heuristic sen-
 355 sitivity depth of $cp/4$ for Love waves in a power-law basin-style velocity pro-
 356 file, given by Haney & Tsai (2020). Taking advantage of the Love wave sen-
 357 sitivity being largely restricted to the basin, we utilize the level-set-tomography
 358 framework of Muir & Tsai (2020) to explicitly define a volume within which
 359 we perform our model updates as part of the model parameterization. The
 360 level-set method implicitly defines boundaries within a domain by taking
 361 them to be a contour interval of a function on that domain (Osher & Sethian,
 362 1988; Gibou et al., 2018). For example, the basin boundary (a 2D surface)
 363 may be defined by the zero-contour of a continuous 3D function. The rough-
 364 ness and topology of the interface can be controlled by the properties of the
 365 underlying function. In our case, by appropriately regularizing the bound-
 366 ary of the inversion volume, we achieve the desired parsimony between the
 367 *a priori* CVM model and constraints from our newly observed data.

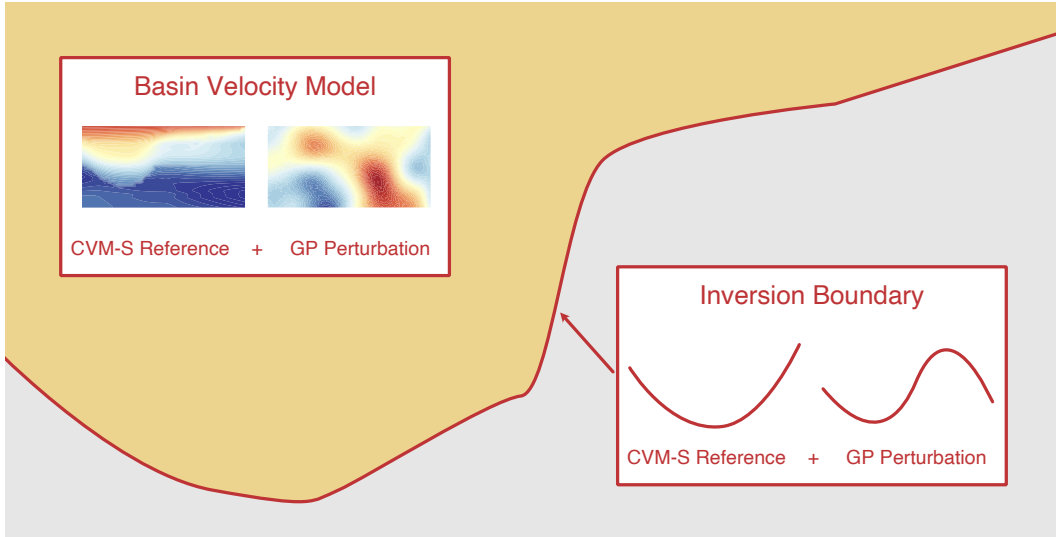


Figure 7.

Schematic of the model definition, showing the construction of the velocity
 model update and the boundary of the inversion, both constructed from a
 CVM-S reference perturbed by a Gaussian Process. The background model,
 schematically shown in grey, is given by the unaltered CVM-S model.

In this study, our model parameterization consists of two parts — a bound-
 ary to the inversion domain, and the velocity perturbations within that do-
 main. Both components of the model are given by Gaussian Processes (GP)
 (Rasmussen & Williams, 2006). GPs are a general method of introducing
 spatial relationships into spatial interpolation, projection and inverse prob-
 lems (Valentine & Sambridge, 2020a,b). In this study we use GPs to reg-
 ularize our inversion, in an analogous way to the spatial damping and smooth-
 ing used in the frequently used Tikhonov regularization framework (Aster
 et al., 2018), although the the smoothing induced by GPs is more flexible
 and easier to interpret. GP models are defined by the property that, for a
 collection of sample points x , the output $f(x)$ of the GP is jointly distributed
 as a multivariate normal distribution. The wide range of choice in defining
 the covariance matrix of the multivariate normal makes the GP modelling
 framework very powerful. For instance, nearly diagonal matrices result in
 highly uncorrelated spatial behaviour, where only the amplitudes of the out-
 put $f(x)$ are affected. Matrices with large off-diagonal components can in-
 troduce interesting spatial covariances in $f(x)$, such as restricting the out-
 put to be smooth up to certain derivatives, include spatial periodicity, pre-
 fer correlation at certain length scales etc.

The pairwise covariance between $f(x)$ and $f(x')$ is given by a covari-
 ance function $C(x, x')$. Given that the covariance function controls the rough-
 ness, characteristic length scale(s) and potential periodicities of the GP, the
 selection of an appropriate covariance function is the most important part
 of GP modelling. We use a Whittle-Matérn covariance function in this study,
 which is a common choice for initial treatment of spatial modelling. The
 Whittle-Matérn covariance allows explicit control over the degree of rough-
 ness, ranging from not-differentiable to infinitely smooth depending on a
 parameter β . The spatial correlations of Whittle-Matérn GPs have a sin-
 gle dominant length scale l . The Whittle-Matérn covariance function is given
 by

$$C(x, x') = \sigma^2 \frac{2^{1-\beta}}{\Gamma(\beta)} \left(\frac{\|x - x'\|_2}{l} \right)^\beta K_\beta \left(\frac{\|x - x'\|_2}{l} \right), \quad (4)$$

where Γ is here the gamma (or extended factorial) function and K_β is the
 modified Bessel function of the second kind. A comprehensive treatment of
 classical GP models, including discussion of other common choices of co-
 variance functions, may be found in Rasmussen & Williams (2006). The sta-
 tistical properties of a GP are controlled by its hyperparameters, which for
 the Whittle-Matérn covariance function are l , the characteristic length scale,
 σ the characteristic scale of perturbations, and β the regularity parameter.
 Individual realizations of GPs using the Whittle-Matérn covariance are $\beta -$
 $\frac{1}{2}$ times continuously differentiable. In practice β is very hard to infer in most
 inverse problems as finite observations are unable to resolve rough details,
 and so it is set to $\beta = 3\frac{1}{2}$ for the remainder of this study. This choice of
 β generates sufficiently smooth models to ensure that Love-wave eigenval-
 ues are correctly calculated, and does not introduce any artificial roughness
 into samples from the posterior distribution that is not warranted by the
 data. We do not set β to any higher value (which would result in greater

smoothness) so that the basin boundary can be sufficiently steep to capture the abrupt change in Love wave amplification.

GP models with variable hyperparameters offer great flexibility, however they are expensive to compute in the spatial domain as they require repeated inversion of the spatial prior covariance matrix C , which is a function of the hyperparameters. The inversion of this dense matrix is in general an operation of complexity $O(n^3)$ for n model evaluation points. To accelerate the GP computations, rather than evaluating the GP at each station and forward model depth grid-point, we approximate the model by defining it on a regular grid with n_{cell} grid nodes in each dimension. Using a structured grid allows us to specify the model by means of its hyperparameters and 3D Fourier coefficients ξ_v and ξ_b for the velocity and inversion boundary components respectively, as is further discussed in the Appendix (Lindgren et al., 2011; Chen et al., 2019). Efficient sampling of the GP can then be performed by an inverse real Fast Fourier Transform (complexity of order $O(3m^3 \log(m))$ where $m = n_{cell}/2 + 1 \ll n$), followed by interpolation by cubic splines to the station locations required for computing the forward model for phase velocity and amplitude underneath each station. We use the same length scale parameter l for both the velocity update and the inversion boundary; the inversion domain is $22 \times 22 \times 12$ km in size, which must be rescaled to a unit cube for the inverse Fourier transform. The inversion area was determined by finding the smallest square that encompassed the stations, and is shown in Figure 2. We use 16 cells in each dimension, and a rescaled \tilde{l} parameter on the unit cube domain, which induces an effective length scale of $l_{xy} \sim 22\tilde{l}$ in the horizontal direction and $l_z \sim 12\tilde{l}$ in the vertical direction – equivalent to assuming vertical heterogeneity has a characteristic length scale half that of lateral heterogeneity. We denote the evaluation (via inverse FFT) of the velocity GP model given velocity Fourier coefficients ξ_v , length scale \tilde{l} and velocity characteristic perturbation amplitude σ_v at a location (x, y, z) by $GPV_{\xi_v, \tilde{l}, \sigma_v}(x, y, z)$, and the evaluation of the inversion boundary given boundary Fourier coefficients ξ_b , length-scale \tilde{l} and boundary characteristic perturbation amplitude σ_b at a location (x, y) by $GPB_{\xi_b, \tilde{l}, \sigma_b}(x, y)$. For both GP models, a Whittle-Matérn covariance function is assumed. We use the CVM-S velocity and basin profile as the reference model which we will perturb during the inversion, to ensure initialization near a physical solution. CVM-S was chosen over CVM-H as the reference due to its smoothness, which lends itself to more concordant velocity models across the inversion boundary, and also because it better fits waveforms within the basin (Lai et al., 2019).

The V_s model is therefore given by

$$V_s(x, y, z) = \begin{cases} V_{\text{CVM-S}}(x, y, z) + GPV_{\xi_v, \tilde{l}, \sigma_v}(x, y, z) & z < z_{\text{CVM-S}}(x, y) + GPB_{\xi_b, \tilde{l}, \sigma_b}(x, y) \\ V_{\text{CVM-S}}(x, y, z) & z \geq z_{\text{CVM-S}}(x, y) + GPB_{\xi_b, \tilde{l}, \sigma_b}(x, y), \end{cases} \quad (5)$$

where $V_{\text{CVM-S}}$ and $z_{\text{CVM-S}}$ are the reference S velocity model and basin edge extracted from CVM-S. CVM-S does not explicitly define a basin edge, and so we discuss how we define the reference basin geometry in Section 3.2. A

graphical schematic of the definition of the discretized model is shown in Figure 7. Density and V_p are then calculated from the V_s model using the empirical relationships of Brocher (2005), which are suitable for basins within southern California.

3.2 Extracting Reference Basin Depth Profiles from CVM-S

The SCEC CVM-S model is defined by a gridded voxel parametrization of V_P , V_S and ρ , i.e., it does not contain explicit definitions of basin boundaries. To obtain reference boundaries for the CVM-S model, we utilized the following procedure. At each depth slice, we computed the mean and standard deviation of V_S . We then flagged each voxel for which V_S was slower than one standard deviation below the mean velocity of that depth slice as a potential basin candidate. For each 1D depth profile, we then worked from the second ($z=500$ m) depth slice downwards, flagging a voxel to be within a basin only if all voxels above it were also flagged. Working from the second depth slice avoids the connection of individual basins due to the large low velocity surface feature in the CVM-S 4.26 model.

This process assumes that basins are strictly convex, which is not true in general but is a useful approximation to begin the inversion process. Using the *scipy* module *ndimage* (SciPy 1.0 Contributors et al., 2020), we then performed image segmentation using the *label* function. This function assigns each connected volume a unique integer index, that can then be used to extract the basin from the larger regional velocity model. This process identified 61 individual basins in southern California, of which the most prominent correspond to the Ventura Basin, combined Los Angeles and San Gabriel basins, San Fernando Basin, and the Salton Trough. This workflow is presented in Figure 8. The boundaries of the Los Angeles / San Gabriel basin candidate were then utilized as the reference basin bottom surface for the inversion step.

3.3 Forward Modelling

In order to predict the data from the final rasterized velocity model given by our model parametrization, we employ the lumped-mass finite element method for surface-wave eigenvalue calculation first proposed by Lysmer (1970), and implemented for Love waves by Haney & Tsai (2020). The rasterized model is interpolated onto a set of finite elements of exponentially increasing thicknesses h given by $h_n = a \min(\lambda) * \exp(N/(na))/n$ where $N = 50$ is the number of layers in the model, $\min(\lambda)$ is the minimum wavelength corresponding to the minimum phase velocity in a reference model, and $a = 0.25$ is the constant used to control the exponential scaling. This exponential scaling heuristically balances the need for finer resolution near the top of the model when calculating shorter period Love waves, against computational efficiency, in a way that is near optimal due to the approximate exponential shape of Love eigenfunctions (Tsai & Atiganyanun, 2014; Haney & Tsai, 2015, 2017, 2020). These layers are stacked on top of 4 layers of thick-

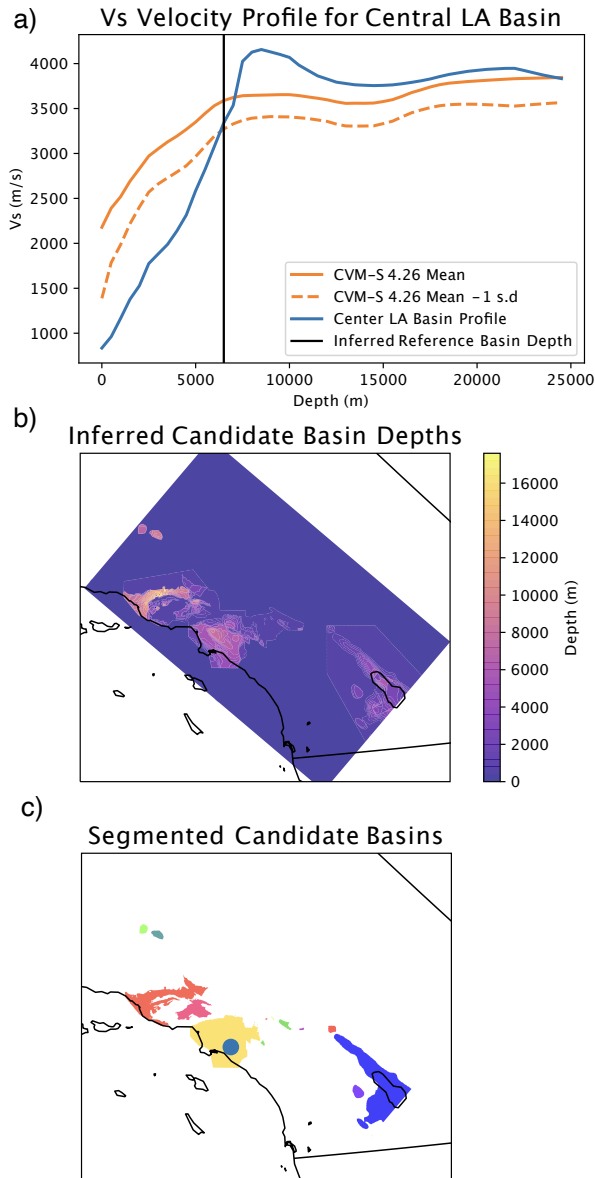
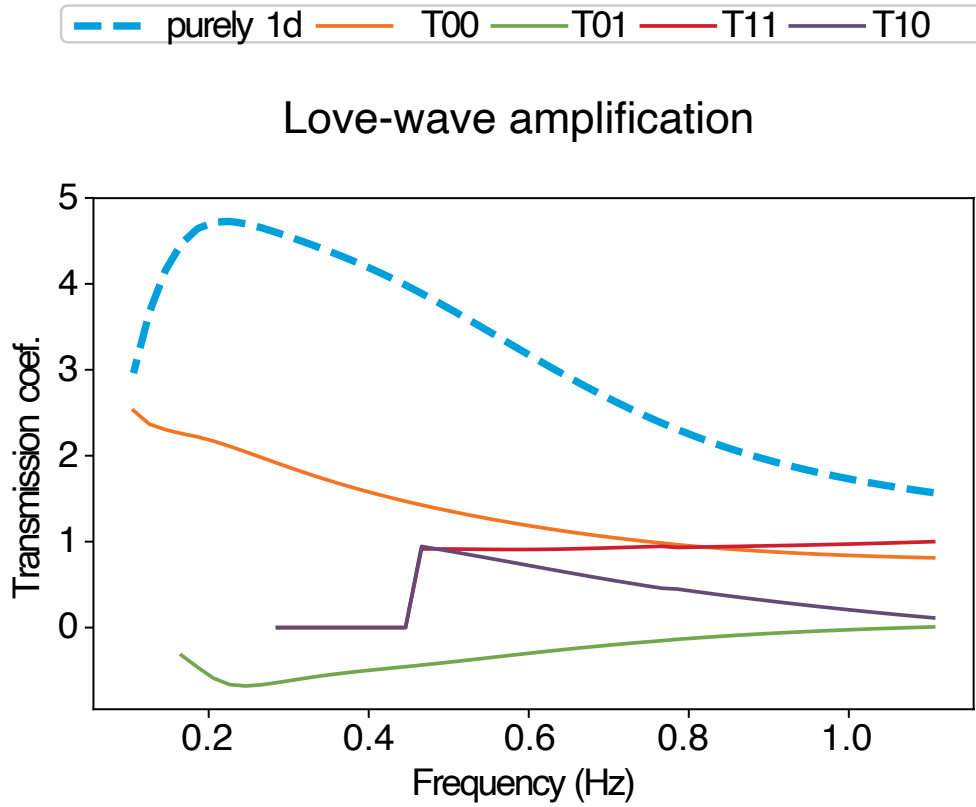


Figure 8.

Outline of steps used to extract a reference basin surface from CVM-S. a) For each vertical profile in CVM-S, we determine where (if anywhere) the V_S profile first becomes faster than one standard deviation below the mean CVM-S velocity at that depth. All depths above this level are set to be a potential candidate basin at the location of the profile. In b), we show the extracted candidate basin depths across southern California. In c), we strip off the top 500 m (which is highly connected) and then use the SciPy *ndimage label* function to segment the remaining data volume by assigning each independent connected volume a unique index. The three major basin families of southern California are clearly seen in pink (Ventura / San Fernando), yellow (Los Angeles / San Gabriel / San Bernardino) and blue (Salton Trough).

**Figure 9.**

Transmission coefficients for a Love wave entering the Los Angeles basin obtained using a 1D mode-coupling theory (Datta, 2018; Brissaud et al., 2020). This represents a worst-case mode-conversion scenario, with the true basin exhibiting a smoother horizontal gradient and hence less conversion. Even in this case, the conversion of energy from the fundamental mode to first overtone T_{01}/T_{00} is relatively small, suggesting that our use of classical Love-amplification theory is appropriate.

ness $h = 10$ km simulating an infinite half-space to avoid contamination with the locked lower boundary condition. We then set up the finite element stiffness and mass matrices as given by Haney & Tsai (2020), and solve for the maximum slowness eigenfunction u that corresponds to the fundamental Love mode as well as the phase velocity c and group velocity c_g . The relative amplification of Love waves directly observed between two locations can then be calculated by

$$\frac{a_1}{a_2} = \left(\frac{c_{g1} I_1}{c_{g2} I_2} \right)^{-1/2}, \quad (6)$$

with $I = \int_0^\infty \rho(z)u(z)^2 dz$ (Bowden & Tsai, 2017; Bowden et al., 2017). Transmission coefficients obtained using a 1D mode-conversion theory (Datta, 2018; Brissaud et al., 2020), applied to Love waves transmitting from a characteristic out-of-basin velocity and density profile to an in-basin profile, are plotted in Figure 9. The results of this mode-conversion test suggest that any potential modelling error from neglecting mode-coupling is small. As we use a derivative-free inversion method, these quantities are sufficient to solve for the optimal model.

3.4 Inverse Solver

We use an extension of the Ensemble Kalman Sampler (EKS, Garbuno-Inigo et al. (2020)) to perform the inversion. This method uses an interacting ensemble of particles that follow Langevin diffusion dynamics to infer a Gaussian approximation to the posterior of the inverse problem. The EKS is derivative-free and embarrassingly parallel in the forward model, which enables rapid user iteration between different datasets and forward modelling methods, as well as easy deployment on heterogenous computing networks. The EKS as outlined in Garbuno-Inigo et al. (2020) assumes that all model parameters have a Gaussian prior. This restricts the model to have fixed hyperparameters (e.g. \tilde{l} , σ_v , σ_b , as required to set the statistical behaviour of the model parameterization described in Section 3.1), which introduces a significant potential for practitioner bias as we do not have a good basis for estimating these *a priori*. Consequently, we have further developed the EKS to handle hierarchical models with variable hyperparameters. The original EKS and our extension to it are discussed in detail in Appendix A. The priors for the velocity hyperparameters are given by $1/\tilde{l} \sim Normal(0, 0.6)$ and $\sigma_v \sim Normal(0, 0.1)$ in scaled inverse km and km/s respectively. Experimentation has shown that the characteristic boundary perturbation amplitude σ_b is not sufficiently identifiable from our data, so we set it to a reasonable value of 0.5 km that is small enough to avoid large, unrealistic changes in the basin geometry while allowing a sufficient fit to the data. Using these hyperparameter priors, we run hierarchical EKS sampling using an initial step length $\Delta t_0 = 50$, and an ensemble size of 32. We double both the step length and the ensemble size every 50 iterations up to iteration 250, and further double the step length only at iteration 300, to finish with 400 iterations. The purpose behind this doubling scheme is to rapidly approach the *maximum a posteriori* (MAP) point using rough gradients from a small num-

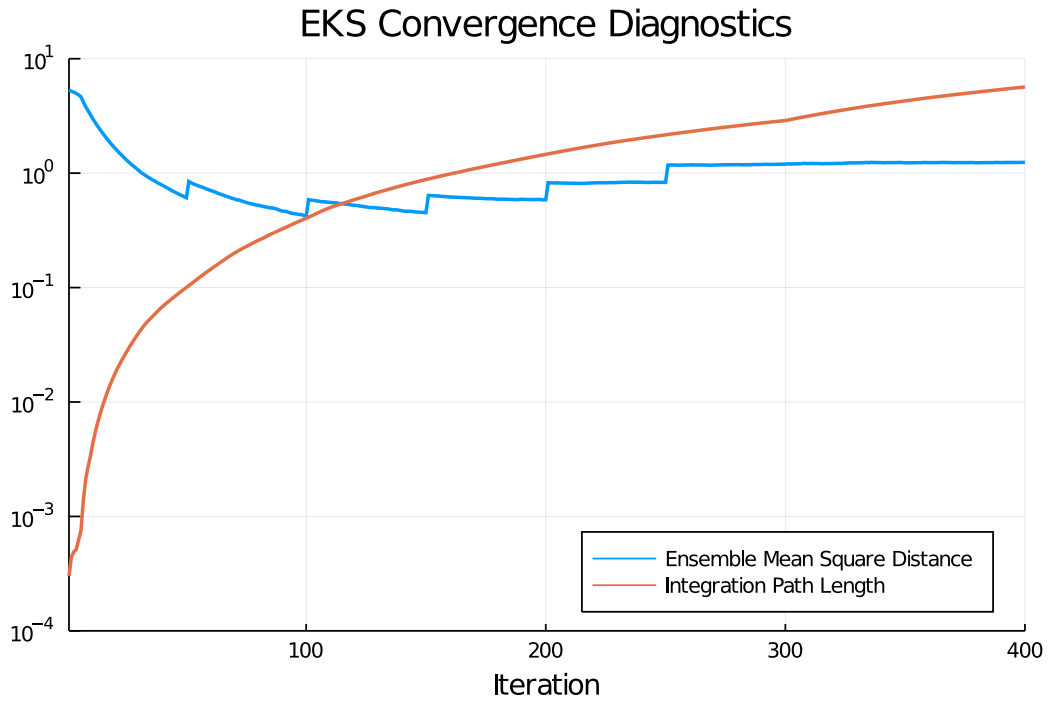


Figure 10.

Convergence diagnostics of the Ensemble Kalman Sampler (EKS) showing the Mean Square Distance between ensemble members converging to a constant, which suggests the ensemble has reached an equilibrium and is approximating the posterior. The integration path length steadily increases, showing that the ensemble is not being forced to take very small steps (heuristics from Garbuno-Inigo et al. (2020) suggest a path length of 2 is sufficient to approximate the posterior).

546 ber of ensemble members, and then perform more accurate sampling of the
 547 posterior using more ensemble members (Garbuno-Inigo et al., 2020). The
 548 step length doubling counteracts the tendency of the gradient amplitude to
 549 be small near the MAP point. Convergence diagnostics for the inversion run
 550 are shown in Figure 10. The final inversion reduced the weighted Gaussian
 551 misfit function from 8.79 (for the CVM-S model) to 5.33, a variance reduc-
 552 tion of 22%, which is a notable improvement from the already highly op-
 553 timized reference model.

554 4 Results and Implications for the Los Angeles Basin

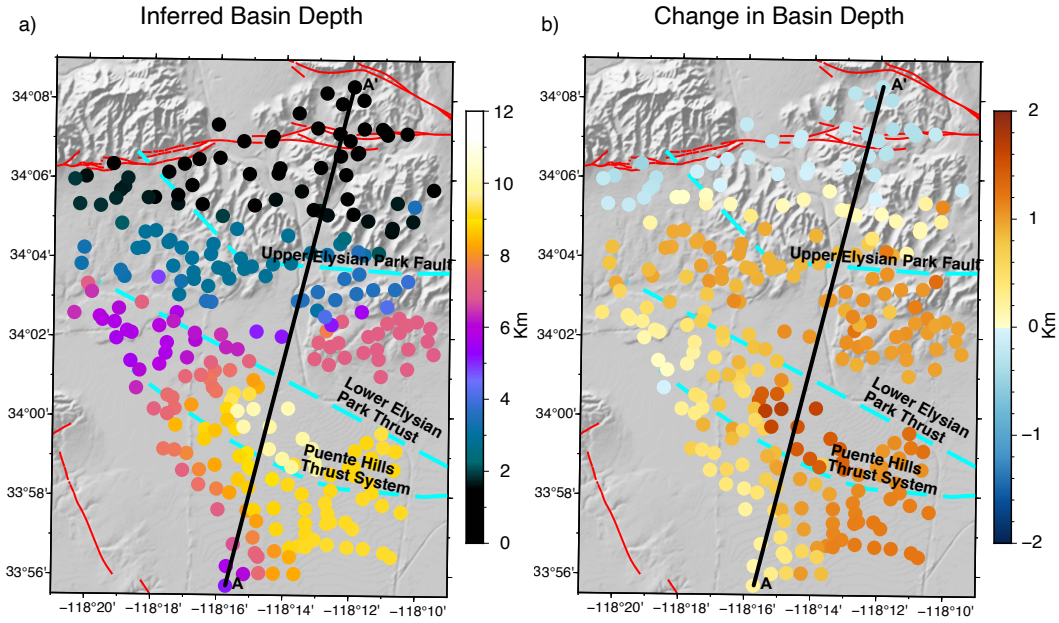


Figure 11.

a) Mean depth of the inferred basin interface from the final ensemble. b) The inferred change in the depth of the Los Angeles Basin relative to CVM-S, showing deepening of the basin especially south of the Upper Elysian Park fault (top thick dashed cyan line), and shallowing of the model in the hilly terrain to the North of the CSN. In both panels, major late Quaternary faults (<130 Kyr) are shown in red, other Quaternary faults are shown in thick dashed cyan. The transect A-A' is shown in black.

555 The results of the inversion are shown in Figures 11, 12 and 13. In Fig-
 556 ure 11 we plot the mean depth to the inferred basin bottom and the inferred
 557 change in the depth of the Los Angeles basin at each station. The change
 558 in basin depth is defined by the difference between the reference basin depth
 559 extracted from CVM-S in Section 3.2, and the depth to the same velocity
 560 contour in the final model. Figure 12 shows the details of the inversion along
 561 profile A-A'. Figure 13 shows the approximate posterior distribution of the
 562 hyperparameters in the inversion. In Figure 12, we also show the reference
 563 CVM-S model used to initialize the inversion, the mean of the EKS ensem-

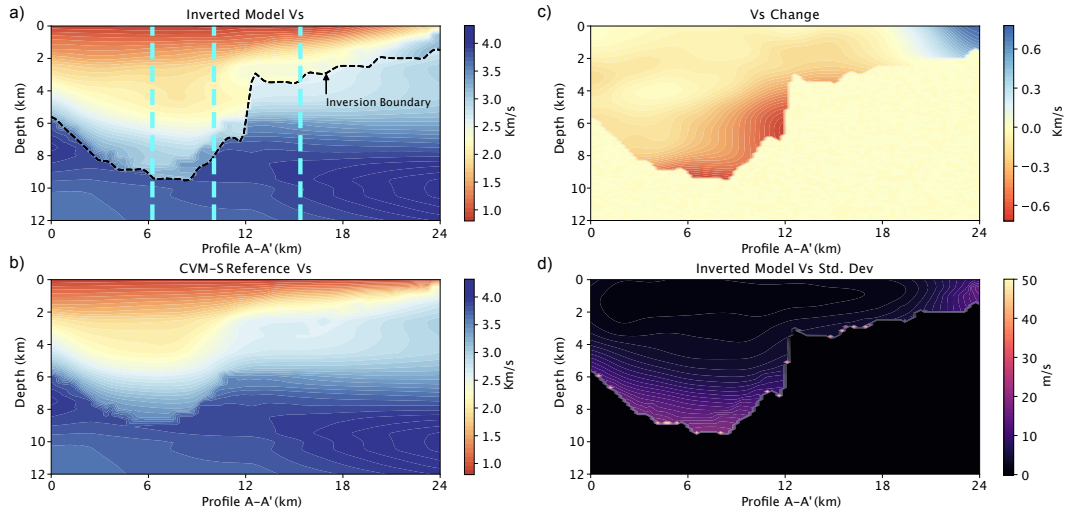


Figure 12.
a) Mean of the final ensemble V_S model, b) CVM-S reference model V_S , c) difference between final model and reference model, d) standard deviation of the final ensemble V_S model.

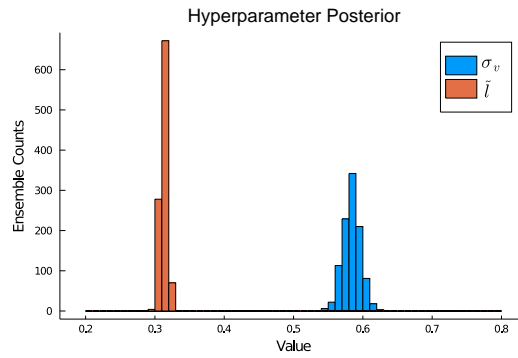


Figure 13.
Approximate posterior distribution from the final ensemble for the hyperparameters \tilde{l} and σ_v .

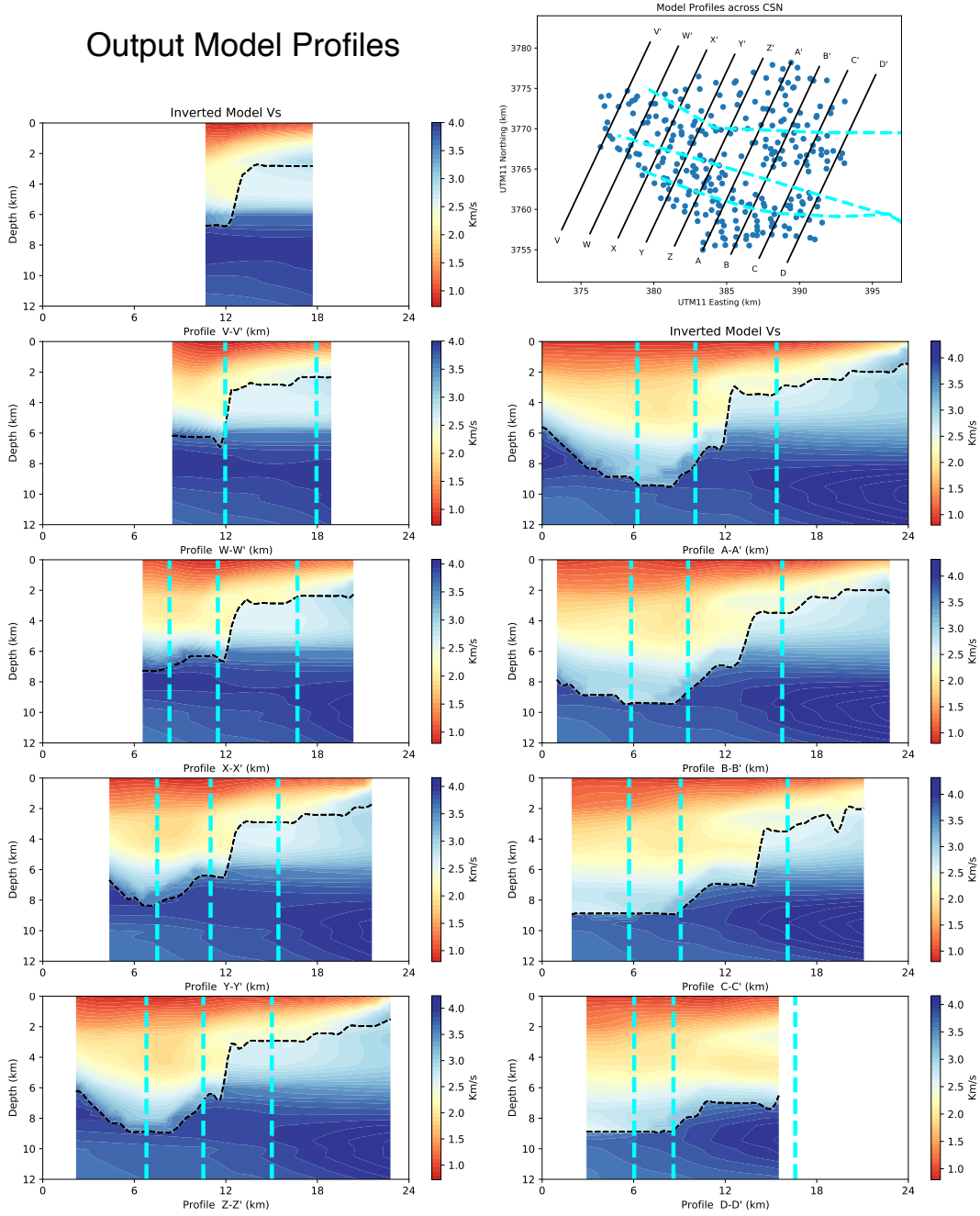


Figure 14. Profiles of the mean output V_s across the Los Angeles Basin, with inferred Quaternary faults in dashed cyan and the inferred edge of the inversion shown in dashed black.

564 ble, the difference between these two, and the standard deviation of the en-
565 semble. The standard deviation gives a sense of the relative uncertainty of
566 the final inversion. As discussed in Garbuno-Inigo et al. (2020), in the low-
567 particle limit EKS sampling cannot fully capture the range of uncertainty
568 in the true inversion posterior, and so the plotted standard deviations are
569 best assessed in a qualitative fashion. The EKS ensemble indicates that the
570 highest uncertainties are along the boundary of the model. Within the in-
571 verted area of the final model, the uncertainties are highest in the deep cen-
572 tral basin where the 4-10 s Love wave period range offers less sensitivity, and
573 near the northeastern edge of the model where the phase velocities are high,
574 resulting in small travel time gradients and hence higher uncertainties when
575 employing eikonal tomography.

576 There are two principle features that are apparent from the results of
577 the inversion. The first and most significant finding is that the data sup-
578 port a deeper Los Angeles basin along its northeastern edge, with an espe-
579 cially large jump in basin depth in the area immediately abutting the Up-
580 per Elysian Park fault as defined in the USGS Quaternary fault map (USGS,
581 2020). The increase in basin depth reaches its maximum just south of down-
582 town LA, as is seen in the southern part of Figure 11 b) which shows the
583 change in basin depth. The Upper Elysian Park fault is shown by a thick
584 dashed cyan line in the center-right of the panels of Figure 11, and demar-
585 cates a steep gradient in the edge of the basin that has been accentuated
586 as a result of the inversion. In Figure 12, this large jump in the depth of
587 the basin edge occurs in the center of the profile A-A', with Figure 12 c)
588 showing that the deep parts of the basin to the SSW of the fault are sig-
589 nificantly slower in our final model, with the edge of the basin being signif-
590 icantly steeper in our model in a) than the reference model in b). This steep-
591 ening is spatially coincident with the observations of high amplification fur-
592 ther north in the data than in the reference models, seen in Figure 3, par-
593 ticularly in the 5–7 s band. Extracting the average basin edge gradient from
594 11.25–13.25 km along profile A–A' in Figure 12 gives a dip angle of 72–73°. The SCEC CVMs have evolved from the original models of Magistrale et al. (1996, 2000). For the Los Angeles basin, an empirically determined velocity law for compacted sediments is used (Faust, 1951). The velocity profiles are controlled by the depth of contacts between two large scale units (the Repettian and Mohnian), the inferred basement depth, and the age of the surface, as reported in Wright (1991). The results of Wright (1991)) rely on geological information from control wells. Wright's work in turn initialized the SCEC CVMs, either as a starting model for full-waveform inversion as used in CVM-S (Lee et al., 2014) or by acting as constraints in CVM-H (Tape et al., 2009; Shaw et al., 2015). There is a notable gap in the location of the control wells across the steep northeastern boundary of the basin that is now covered by the CSN, leading to uncertainty about the basin geometry in prior works. Given the position of the basin sidewall is situated between the imbricated blind-thrust faults of the Elysian Park system (Plesch et al., 2007), the high apparent dip angle imaged by surface-wave measurements gives further support to an over-thrusted basin in this region (as is

611 included in the CVM-H model, albeit further to the northeast than is sug-
 612 gested by our results). Further cross-sections through the model are shown
 613 in Figure 14, and show that this steep basin sidewall continues along the
 614 northwest-southeast axis of the northern LA basin wall.

615 The second notable finding is that the depth of the low velocity zone
 616 in the hilly terrain north of the Los Angeles basin is substantially shallower
 617 than in the reference model, which can be seen both along the northern edge
 618 of Figure 11 and in the faster velocities around end A' of the transect in Fig-
 619 ure 12 c). This shallowing of the basin relative to the CVM-S model is to
 620 be expected given the high Love wave speeds recorded in the northeast of
 621 the array from eikonal tomography, and the relatively lower amplification
 622 when compared to the slow, deep sediments in the central basin. Indeed,
 623 the northeastern components of the CSN operate within the surface expres-
 624 sion of the lower Puente and Topanga units of the LA basin stratigraphic
 625 column, which were assembled early within the LA basin sequence and sup-
 626 port a shallow sequence of basin rocks towards to the right of profile A-A'
 627 (Yerkes et al., 2005). In the Supplement, we further discuss these two main
 628 features in the context of fitting the rule-based CVM1 (Magistrale et al.,
 629 1996, 2000) to profile A-A'. By perturbing the locations of the loosely con-
 630 strained geological contacts that define the CVM1, we analyse the outcomes
 631 of our fully 3D inversion in terms of geological structure, and find that the
 632 steep basin sidewall is consistent with recently (≤ 4 Ma) active deformation.

633 5 Conclusion

634 We use Love waves generated by the Mw 6.4 and Mw 7.1 Ridgecrest,
 635 CA earthquakes to obtain Love-wave phase velocities and relative ampli-
 636 tudes between 4–10 s period using the Caltech-LAUSD Community Seis-
 637 mic Network, which offers unprecedented high-density coverage of the north-
 638 east LA basin. We use the level-set method of Muir & Tsai (2020) to de-
 639 velop a parsimonious velocity inversion that updates the SCEC CVM-S back-
 640 ground model only where empirical estimates of data uncertainty indicate
 641 additional complexity is warranted. By employing fully 3D surface-wave in-
 642 version, we avoid internal artifacts in the model and make best use of a re-
 643 latively small dataset. In doing so, we find that the northeast wall of the LA
 644 basin is substantially steeper than that of the CVM-S model, allowing for
 645 high amplifications of surface waves in the 4–6 s period band travelling within
 646 the basin. The constraints provided by this model cover some of the parts
 647 of LA with the highest density of population, infrastructure and commer-
 648 cial development, and highlight the continued importance of seismic veloc-
 649 ity model evolution in providing the most accurate possible estimates of po-
 650 tential strong ground motions in this important city.

651 Acknowledgments

652 The authors would like to thank Rob Graves (USGS) for providing synthetic
 653 seismograms for the Ridgecrest events. This study was supported by the
 654 United States National Science Foundation awards EAR-1520081, EAR-2105358

and EAR-2011079, and the Southern California Earthquake Center award 20024. JBM acknowledges the support of the General Sir John Monash Foundation and the Origin Energy Foundation for support during his graduate studies. The CSN data used in this paper are freely available from <http://csn.caltech.edu/data>. The TEKS inversion code may be found at <https://github.com/jbmuir/TikhonovEnsembleKalmanSampling.jl>. Data analysis codes can be found at <https://github.com/jbmuir/CSN-Ridgecrest>.

Appendix A Hierarchical Ensemble Kalman Sampler

The Ensemble Kalman Inversion (EKI) scheme was introduced by Iglesias et al. (2013) by deriving a state-variable augmented Ensemble Kalman Filter (Evensen, 1994, 2003) with dynamics that approximated the Levenberg-Marquardt method. EKI acts as an efficient black-box optimizer for large scale PDE constrained problems for which it is intractable or infeasible to obtain gradients, and has been used successfully in practical geophysical applications (e.g. Muir & Tsai (2020); Tso et al. (2021)). Subsequent to its initial formulation, much analysis on the EKI scheme has been performed by studying it as a continuous time gradient flow (Kovachki & Stuart, 2018), rather than in its original formulation as a discrete time dynamical system. This has led to the development of the Ensemble Kalman Sampler (EKS, Garbuno-Inigo et al. (2020)), an algorithm for approximate sampling of the posterior distributions of large-scale Bayesian PDE constrained inverse problems. We utilize a hierarchical variant of the EKS scheme in this study to sample the posterior distribution of our local model update — we will briefly reintroduce the EKS scheme as described in Garbuno-Inigo et al. (2020) and then outline our variant hierarchical formulation. In general, the objective of these schemes is to approximate a posterior distribution whose negative log-posterior is of the form

$$\Phi(u, d) = \|d - G(u)\|_{\Gamma} + R(u), \quad (\text{A1})$$

where Γ is the data noise covariance matrix, and where the regularization term $R(u)$ introduces prior information. For instance, a typical choice would be a Tikhonov style regularization term $R(u) = \|u\|_{C_0}$ for some prior covariance matrix C_0 . The norms here are defined by $\|u\|_A = \langle u, u \rangle_A = u^T A^{-1} u$.

The EKS scheme is an ensemble-based approximation of a preconditioned overdamped Langevin equation, which is a stochastic differential equation (SDE) of the form

$$\dot{u} = -C(u)\nabla_u\Phi(u) + \sqrt{2C(u)}\dot{W} \quad (\text{A2})$$

with $C(u)$ a preconditioning operator that depends on u and \dot{W} a Brownian motion term. It can be shown that the long-term behavior of this SDE gives rise to a trajectory that has a distribution given by $p(u|d) \propto \exp(-\Phi(u, d))$ — i.e. the desired target posterior (Gelman et al., 1997). In the EKS scheme, an ensemble of particles $U = \{u^{(j)}\}_{j=1}^J$ are used to approximate the gradient of the likelihood, and $C(u)$ is chosen to be the empirical covariance $C(U) = \frac{1}{J} \sum_{j=1}^J (u^{(j)} - \bar{u})(u^{(j)} - \bar{u})^T$, where overbars denote means across

698 the particle ensemble. Preconditioning by the empirical covariance acts to
 699 approximate the local curvature of the posterior by the ensemble, giving ac-
 700 celerated convergence compared to the unconditioned equation in a simi-
 701 lar manner to the difference between Newton’s method and gradient descent.
 702 The dynamics of this system of particles are given by the following SDE (with-
 703 out the gradient approximation and for Tikhonov-style Gaussian priors)

$$\dot{u}^{(j)} = \frac{1}{J} \sum_{k=1}^J \langle (\nabla_u G(u^{(j)})(u^{(k)} - \bar{u}), G(u^{(j)} - d) \rangle_{\Gamma} u^{(k)} - C(U)C_0^{-1}u^{(j)} + \sqrt{2C(U)}\dot{W}^{(j)}. \quad (\text{A3})$$

704 Making the ensemble approximation for the gradient of the forward oper-
 705 ator G allows us to rewrite this in a form without an explicit derivative:
 706

$$\dot{u}^{(j)} = \frac{1}{J} \sum_{k=1}^J \langle (G(u^{(k)}) - \bar{G}, G(u^{(j)} - d) \rangle_{\Gamma} u^{(k)} - C(U)C_0^{-1}u^{(j)} + \sqrt{2C(U)}\dot{W}^{(j)}, \quad (\text{A4})$$

707 which is the equation solved by the EKS as described by Garbuno-Inigo et
 708 al. (2020). We will define $D(U) = \frac{1}{J} \sum_{k=1}^J \langle (G(u^{(k)}) - \bar{G}, G(u^{(j)} - d) \rangle_{\Gamma}$ for
 709 future convenience, so that the dynamics for the whole ensemble are given
 710 by
 711

$$\dot{U} = UD(U)^T - C(U)C_0^{-1}U + \sqrt{2C(U)}\dot{W}. \quad (\text{A5})$$

712 We note that at the equilibrium of the ensemble where $\dot{U} \sim 0$, these dy-
 713 namics heuristically suggest a balance between a Newton-style update of
 714 the ensemble (using an empirical covariance matrix to approximate the in-
 715 verse Hessian), which will converge to the maximum *a posteriori* point, and
 716 the generation of correlated Gaussian noise scaled to the original ensemble.
 717 The average behavior of the ensemble at equilibrium therefore results in sam-
 718 pling a local Gaussian approximation of the posterior. A video illustrating
 719 the evolution of the ensemble for a toy problem is available in the supple-
 720 ment.
 721

722 In geophysical problems the scale of appropriate regularization (i.e., the
 723 choice of operator C_0 for Tikhonov regularized problems) is often unknown.
 724 As such, much recent effort has been devoted to the development of hier-
 725 archical methods for solving inverse problems, in which the prior itself is to
 726 some degree unknown and is controlled by some number of hyperparame-
 727 ters (see e.g. Malinverno & Briggs (2004)). Additionally, for large-scale prob-
 728 lems with Gaussian priors, it may be beneficial for efficient sampling to per-
 729 form a coordinate transformation into diagonalized coordinates that remove
 730 the correlations in the prior between hyperparameters and the main param-
 731 eters used in the inverse problem, as will be described below. These parametriza-
 732 tions are known as whitened, non-centered hierarchical parametrizations (Chada,
 733 2018; Chada et al., 2018; Chen et al., 2019). The set of parameters is given
 734 by a collection of “regular” parameters ξ and hyperparameters θ . For zero-
 735 mean Gaussian priors, the coordinate transformation is given by $u = L(\theta)\xi$
 736 for a Cholesky factor $C_0(\theta) = L(\theta)L(\theta)^T$. With this transformation, the
 737 prior for the parameters ξ is simply a Gaussian with identity covariance ma-
 738 trix. The Cholesky decomposition is an expensive operation of order $O(N(\xi)^3)$

739 where $N(\xi)$ is the number of main parameters. Lindgren et al. (2011) showed
 740 explicitly how to approximate the coordinate transformations used in this
 741 study by solving a stochastic partial differential equation (SPDE), which
 742 can be substantially more efficient. For certain choices of prior covariance,
 743 and by defining known boundary conditions on a rectangular volume en-
 744 compassing the model parameters, there are known analytic solutions for
 745 the appropriate eigenfunctions $\phi_i(\theta)$ and eigenvalues $\nu_i(\theta)$ with which to solve
 746 the SPDE such that truncation of the series of eigenfunctions has the small-
 747 est total mean squared error; these eigenfunction-eigenvalue pairs form the
 748 Karhunen-Loève (KL) expansion (Dashti & Stuart, 2013). Using the KL ex-
 749 pansion, $L(\theta)\xi \sim \sqrt{\nu_i(\theta)}\phi_i(\theta)\xi_i$. Using these known analytic eigenfunc-
 750 tions and appropriately truncating the KL expansion to a reasonable num-
 751 ber of eigenfunctions can drastically increase the speed of performing the
 752 coordinate transformation; for the commonly used Whittle-Matérn family
 753 of covariance functions in a rectangular domain, the transform (assuming
 754 Neumann boundary conditions) can be calculated using the inverse discrete
 755 cosine transform for even greater efficiency (Chen et al., 2019).

756 The hyperparameters θ may have arbitrary priors ρ , which are typi-
 757 cally non-Gaussian but do not depend on ξ ; consequently the dynamics of
 758 the system follow (for ensembles $\Xi = \{\xi^{(j)}\}_{j=1}^J$, $\Theta = \{\theta^{(j)}\}_{j=1}^J$)

$$759 \quad \dot{\Xi} = \Xi D(L(\Theta)\Xi)^T - C(\Xi)\Xi + \sqrt{2C(\Xi)}\dot{W} \quad (\text{A6})$$

$$760 \quad \dot{\Theta} = \Theta D(L(\Theta)\Xi)^T + C(\Theta)\nabla_{\theta} \log(\rho(\Theta)) + \sqrt{2C(\Theta)}\dot{W}. \quad (\text{A7})$$

762 These dynamics derive from the original EKS by considering an augmented
 763 state vector $u = [\xi, \theta]^T$ and allowing arbitrary priors, noting that for a stan-
 764 dard Normal prior $\log(\rho(x)) = (-x^2 - \log(2\pi))/2$, so $\frac{\log(\rho(x))}{\partial x} = -x$. We
 765 have furthermore neglected the cross-covariance terms $\text{Cov}(\Xi, \Theta)$ and as-
 766 sumed a block-diagonal form for the preconditioning matrix, allowing us to
 767 decouple the dynamics as above. In order to solve these equations, we use
 768 the same split-step implicit scheme as Garbuno-Inigo et al. (2020), which
 769 is given by

$$770 \quad \Xi_{k+1}^* = \Xi_k - \Delta t_k \Xi_k D(L(\Theta_k)\Xi_k)^T - \Delta t_k C(\Xi_k)\Xi_{k+1}^* \quad (\text{A8})$$

$$771 \quad \Theta_{k+1}^* = \Theta_k - \Delta t_k \Theta_k D(L(\Theta_k)\Xi_k)^T + \Delta t_k C(\Theta_k)\nabla_{\theta} \log(\rho(\Theta_{k+1}^*)) \quad (\text{A9})$$

$$772 \quad \Xi_{k+1} = \Xi_{k+1}^* + \sqrt{2\Delta t_k C(\Xi_k)}W(\Xi)_k \quad (\text{A10})$$

$$773 \quad \Theta_{k+1} = \Theta_{k+1}^* + \sqrt{2\Delta t_k C(\Theta_k)}W(\Theta)_k, \quad (\text{A11})$$

775 where $W(\Xi)_k$ and $W(\Theta)_k$ are matrices of standard random normals of the
 776 same shape as Ξ and Θ respectively. The timestep Δt_k is calculated adap-
 777 tively following Kovachki & Stuart (2018). Given a reference timestep Δt_0
 778 we have $\Delta t_k = \Delta t_0 / (||D(L(\Theta_k)\Xi_k)|| + \delta)$ where the norm on D is the Frobe-
 779 nius norm and δ is an arbitrary positive constant. Unlike in Garbuno-Inigo
 780 et al. (2020), the inclusion of arbitrary non-Gaussian priors for the hyper-
 781 parameters θ means that the implicit update is no longer linear, but as the
 782 dimension of θ is usually small, the cost of performing this update using an
 783 iterative nonlinear solver is normally not overly burdensome. In practice we

784 use forward-mode automatic differentiation for arbitrary priors ρ and the
 785 L-BFGS method (Liu & Nocedal, 1989) for solving the implicit update for
 786 Θ .

787 References

- 788 Ajala, R., & Persaud, P. (2021, October). Effect of Merging Multiscale Models on
 789 Seismic Wavefield Predictions Near the Southern San Andreas Fault. *Journal of*
 790 *Geophysical Research: Solid Earth*, *126*(10), e2021JB021915.
- 791 Aster, R. C., Borchers, B., & Thurber, C. H. (2018). *Parameter estimation and in-*
 792 *verse problems*. Elsevier.
- 793 Bowden, D. C., & Tsai, V. C. (2017, January). Earthquake ground motion am-
 794 plification for surface waves: Ground Motions for Surface Waves. *Geophysical Re-*
 795 *search Letters*, *44*(1), 121–127. doi: 10.1002/2016GL071885
- 796 Bowden, D. C., Tsai, V. C., & Lin, F. C. (2015, March). Site amplification, at-
 797 tenuation, and scattering from noise correlation amplitudes across a dense ar-
 798 ray in Long Beach, CA. *Geophysical Research Letters*, *42*(5), 1360–1367. doi:
 799 10.1002/2014GL062662
- 800 Bowden, D. C., Tsai, V. C., & Lin, F.-C. (2017, December). Amplification and
 801 Attenuation Across USArray Using Ambient Noise Wavefront Tracking: USAr-
 802 ray Noise Amplitudes. *Journal of Geophysical Research: Solid Earth*, *122*(12),
 803 10,086–10,101. doi: 10.1002/2017JB014804
- 804 Brissaud, Q., Bowden, D. C., & Tsai, V. C. (2020, June). Extension of the
 805 Basin Rayleigh-Wave Amplification Theory to Include Basin-Edge Effects.
 806 *Bulletin of the Seismological Society of America*, *110*(3), 1305–1322. doi:
 807 10.1785/0120190161
- 808 Brocher, T. A. (2005, December). Empirical relations between elastic wavespeeds
 809 and density in the earth’s crust. *Bulletin of the Seismological Society of America*,
 810 *95*(6), 2081–2092. doi: 10.1785/0120050077
- 811 Castellanos, J. C., Clayton, R. W., & Juarez, A. (2020, May). Using a Time-
 812 Based Subarray Method to Extract and Invert Noise-Derived Body Waves at Long
 813 Beach, California. *Journal of Geophysical Research: Solid Earth*, *125*(5). doi:
 814 10.1029/2019JB018855
- 815 Chada, N. K. (2018, January). Analysis of Hierarchical Ensemble Kalman Inversion.
 816 *arXiv:1801.00847 [math]*.
- 817 Chada, N. K., Iglesias, M. A., Roininen, L., & Stuart, A. M. (2018, May). Parame-
 818 terizations for ensemble Kalman inversion. *Inverse Problems*, *34*(5), 055009. doi:
 819 10.1088/1361-6420/aab6d9
- 820 Chen, V., Dunlop, M. M., Papaspiliopoulos, O., & Stuart, A. M. (2019, March).
 821 Dimension-Robust MCMC in Bayesian Inverse Problems. *arXiv:1803.03344*
 822 *[stat]*.
- 823 Clayton, R. W., Heaton, T., Chandy, M., Krause, A., Kohler, M., Bunn, J., ...
 824 Aivazis, M. (2012, January). Community Seismic Network. *Annals of Geophysics*,
 825 *54*(6), 738–747. doi: 10.4401/ag-5269
- 826 Clayton, R. W., Kohler, M., Guy, R., Bunn, J., Heaton, T., & Chandy, M.
 827 (2020, March). CSN-LAUSD Network: A Dense Accelerometer Network in
 828 Los Angeles Schools. *Seismological Research Letters*, *91*(2A), 622–630. doi:
 829 10.1785/0220190200
- 830 Dashti, M., & Stuart, A. M. (2013, February). The Bayesian Approach To Inverse
 831 Problems. *arXiv:1302.6989 [math]*.
- 832 Datta, A. (2018, March). SWRT: A package for semi-analytical solutions of surface
 833 wave propagation, including mode conversion, across transversely aligned vertical
 834 discontinuities. *Geoscientific Instrumentation, Methods and Data Systems*, *7*(1),
 835 101–112. doi: 10.5194/gi-7-101-2018

- 836 Evensen, G. (1994). Sequential data assimilation with a nonlinear quasi-geostrophic
837 model using Monte Carlo methods to forecast error statistics. *Journal of Geophys-*
838 *ical Research*, *99*(C5), 10143. doi: 10.1029/94JC00572
- 839 Evensen, G. (2003, November). The Ensemble Kalman Filter: Theoretical formu-
840 lation and practical implementation. *Ocean Dynamics*, *53*(4), 343–367. doi: 10
841 .1007/s10236-003-0036-9
- 842 Faust, L. Y. (1951, April). Seismic velocity as a function of depth and geologic time.
843 *GEOPHYSICS*, *16*(2), 192–206. doi: 10.1190/1.1437658
- 844 Fichtner, A., van Herwaarden, D.-P., Afanasiev, M., Simuté, S., Krischer, L.,
845 Çubuk-Sabuncu, Y., ... Igel, H. (2018, May). The Collaborative Seismic Earth
846 Model: Generation 1. *Geophysical Research Letters*, *45*(9), 4007–4016. doi:
847 10.1029/2018GL077338
- 848 Filippitzi, F., Kohler, M. D., Heaton, T. H., Graves, R. W., Clayton, R. W.,
849 Guy, R. G., ... Chandy, K. M. (2021, April). Ground motions in urban Los
850 Angeles from the 2019 Ridgecrest earthquake sequence. *Earthquake Spectra*,
851 *875529302110039*. doi: 10.1177/87552930211003916
- 852 Garbuno-Inigo, A., Hoffmann, F., Li, W., & Stuart, A. M. (2020, January). In-
853 teracting Langevin Diffusions: Gradient Structure and Ensemble Kalman Sam-
854 pler. *SIAM Journal on Applied Dynamical Systems*, *19*(1), 412–441. doi:
855 10.1137/19M1251655
- 856 Gelman, A., Gilks, W. R., & Roberts, G. O. (1997, February). Weak convergence
857 and optimal scaling of random walk Metropolis algorithms. *The Annals of Applied*
858 *Probability*, *7*(1). doi: 10.1214/aoap/1034625254
- 859 Gibou, F., Fedkiw, R., & Osher, S. (2018, January). A review of level-set meth-
860 ods and some recent applications. *Journal of Computational Physics*, *353*, 82–109.
861 doi: 10.1016/j.jcp.2017.10.006
- 862 Graves, R. W. (1996). Simulating Seismic Wave Propagation in 3D Elastic Media
863 Using Staggered-Grid Finite Differences. *Bulletin of the Seismological Society of*
864 *America*, *86*(4), 1091–1106.
- 865 Graves, R. W., & Pitarka, A. (2010, October). Broadband Ground-Motion Simu-
866 lation Using a Hybrid Approach. *Bulletin of the Seismological Society of America*,
867 *100*(5A), 2095–2123. doi: 10.1785/0120100057
- 868 Haney, M. M., & Tsai, V. C. (2015, November). Nonperturbational surface-wave
869 inversion: A Dix-type relation for surface waves. *GEOPHYSICS*, *80*(6), EN167-
870 EN177. doi: 10.1190/geo2014-0612.1
- 871 Haney, M. M., & Tsai, V. C. (2017, May). Perturbational and nonperturbational in-
872 version of Rayleigh-wave velocities. *GEOPHYSICS*, *82*(3), F15-F28. doi: 10.1190/
873 geo2016-0397.1
- 874 Haney, M. M., & Tsai, V. C. (2020, January). Perturbational and nonperturbational
875 inversion of Love-wave velocities. *GEOPHYSICS*, *85*(1), F19-F26. doi: 10.1190/
876 geo2018-0882.1
- 877 Iglesias, M. A., Law, K. J. H., & Stuart, A. M. (2013, April). Ensemble Kalman
878 methods for inverse problems. *Inverse Problems*, *29*(4), 045001. doi: 10.1088/0266
879 -5611/29/4/045001
- 880 Ingersoll, R. V., & Rumelhart, P. E. (1999). Three-stage evolution of the Los Ange-
881 les basin, southern California. *Geology*, *27*(7), 593–596.
- 882 Jia, Z., & Clayton, R. W. (2021, May). Determination of Near Surface Shear-Wave
883 Velocities in the Central Los Angeles Basin With Dense Arrays. *Journal of Geo-*
884 *physical Research: Solid Earth*, *126*(5). doi: 10.1029/2020JB021369
- 885 Kohler, M. D., Filippitzi, F., Heaton, T., Clayton, R. W., Guy, R., Bunn, J., &
886 Chandy, K. M. (2020, November). 2019 Ridgecrest Earthquake Reveals Areas of
887 Los Angeles That Amplify Shaking of High-Rises. *Seismological Research Letters*,
888 *91*(6), 3370–3380. doi: 10.1785/0220200170
- 889 Kovachki, N. B., & Stuart, A. M. (2018, August). Ensemble Kalman Inversion:

- 890 A Derivative-Free Technique For Machine Learning Tasks. *arXiv:1808.03620 [cs,*
891 *math, stat]*.
- 892 Lai, V. H., Graves, R., Zhan, Z., Yu, C., & Helmberger, D. (2019). Analyzing Shal-
893 low Basin Effects in Los Angeles Basin using 3D Simulations and Dense Array
894 Analysis. In *SCEC Annual Meeting* (Vol. Contribution 9804).
- 895 Lai, V. H., Graves, R. W., Yu, C., Zhan, Z., & Helmberger, D. V. (2020, October).
896 Shallow Basin Structure and Attenuation Are Key to Predicting Long Shaking
897 Duration in Los Angeles Basin. *Journal of Geophysical Research: Solid Earth,*
898 *125*(10). doi: 10.1029/2020JB019663
- 899 Lee, E.-J., Chen, P., Jordan, T. H., Maechling, P. B., Denolle, M. A. M., &
900 Beroza, G. C. (2014). Full-3-D tomography for crustal structure in South-
901 ern California based on the scattering-integral and the adjoint-wavefield meth-
902 ods. *Journal of Geophysical Research: Solid Earth,* *119*(8), 6421–6451. doi:
903 10.1002/2014JB011346
- 904 Lin, F.-C., Li, D., Clayton, R. W., & Hollis, D. (2013, July). High-resolution 3D
905 shallow crustal structure in Long Beach, California: Application of ambient noise
906 tomography on a dense seismic array. *GEOPHYSICS,* *78*(4), Q45–Q56. doi:
907 10.1190/geo2012-0453.1
- 908 Lin, F.-C., & Ritzwoller, M. H. (2011, September). Helmholtz surface wave to-
909 mography for isotropic and azimuthally anisotropic structure: Helmholtz surface
910 wave tomography. *Geophysical Journal International,* *186*(3), 1104–1120. doi:
911 10.1111/j.1365-246X.2011.05070.x
- 912 Lin, F.-C., Ritzwoller, M. H., & Snieder, R. (2009, June). Eikonal tomography:
913 Surface wave tomography by phase front tracking across a regional broad-band
914 seismic array. *Geophysical Journal International,* *177*(3), 1091–1110. doi:
915 10.1111/j.1365-246X.2009.04105.x
- 916 Lin, F. C., Tsai, V. C., & Schmandt, B. (2014, August). 3-D crustal structure of
917 the western United States: Application of Rayleigh-wave ellipticity extracted from
918 noise cross-correlations. *Geophysical Journal International,* *198*(2), 656–670. doi:
919 10.1093/gji/ggu160
- 920 Lindgren, F., Rue, H., & Lindström, J. (2011, September). An explicit link between
921 Gaussian fields and Gaussian Markov random fields: The stochastic partial dif-
922 ferential equation approach: Link between Gaussian Fields and Gaussian Markov
923 Random Fields. *Journal of the Royal Statistical Society: Series B (Statistical*
924 *Methodology),* *73*(4), 423–498. doi: 10.1111/j.1467-9868.2011.00777.x
- 925 Liu, D. C., & Nocedal, J. (1989, August). On the limited memory BFGS method for
926 large scale optimization. *Mathematical Programming,* *45*(1-3), 503–528. doi: 10
927 .1007/BF01589116
- 928 Lysmer, J. (1970). Lumped Mass Method for Rayleigh Waves. *Bulletin of the Seis-*
929 *mological Society of America,* *60*(1), 89–&.
- 930 Magistrale, H., Day, Steven, Clayton, Robert W., & Graves, Robert. (2000, Decem-
931 ber). The SCEC Southern California Reference Three-Dimensional Seismic Ve-
932 locity Model Version 2. *Bulletin of the Seismological Society of America,* *90*(6B),
933 S65–S76. doi: 10.1785/0120000510
- 934 Magistrale, H., McLaughlin, K., & Day, S. (1996, August). A geology-based 3D ve-
935 locity model of the Los Angeles basin sediments. *Bulletin of the Seismological So-*
936 *ciety of America,* *86*(4), 1161–1166.
- 937 Malinverno, A., & Briggs, V. A. (2004, July). Expanded uncertainty quantification
938 in inverse problems: Hierarchical Bayes and empirical Bayes. *Geophysics,* *69*(4),
939 1005–1016. doi: 10.1190/1.1778243
- 940 Muir, J. B., & Tsai, V. C. (2020, February). Geometric and level set tomography
941 using ensemble Kalman inversion. *Geophysical Journal International,* *220*(2), 967–
942 980. doi: 10.1093/gji/ggz472
- 943 Osher, S., & Sethian, J. A. (1988, November). Fronts propagating with curvature-

- 944 dependent speed: Algorithms based on Hamilton-Jacobi formulations. *Journal of*
 945 *Computational Physics*, 79(1), 12–49. doi: 10.1016/0021-9991(88)90002-2
- 946 Pitarka, A., Graves, R. W., & Rodgers, A. J. (2019, December). Strong Ground Mo-
 947 tion Simulation for the M7.1, 2019 Ridgecrest California Earthquake. *AGU Fall*
 948 *Meeting Abstracts*, 31.
- 949 Plesch, A., Shaw, J. H., Benson, C., Bryant, W. A., Carena, S., Cooke, M., ...
 950 Yeats, R. (2007, December). Community Fault Model (CFM) for Southern Cal-
 951 ifornia. *Bulletin of the Seismological Society of America*, 97(6), 1793–1802. doi:
 952 10.1785/0120050211
- 953 Qiu, H., Lin, F.-C., & Ben-Zion, Y. (2019, September). Eikonal Tomography of
 954 the Southern California Plate Boundary Region. *Journal of Geophysical Research:*
 955 *Solid Earth*, 124(9), 9755–9779. doi: 10.1029/2019JB017806
- 956 Rasmussen, C. E., & Williams, C. K. I. (2006). *Gaussian processes for machine*
 957 *learning*. Cambridge, Mass: MIT Press.
- 958 SciPy 1.0 Contributors, Virtanen, P., Gommers, R., Oliphant, T. E., Haberland, M.,
 959 Reddy, T., ... van Mulbregt, P. (2020, March). SciPy 1.0: Fundamental algo-
 960 rithms for scientific computing in Python. *Nature Methods*, 17(3), 261–272. doi:
 961 10.1038/s41592-019-0686-2
- 962 Shaw, J. H., Plesch, A., Tape, C., Suess, M. P., Jordan, T. H., Ely, G., ... Munster,
 963 J. (2015, April). Unified Structural Representation of the southern California
 964 crust and upper mantle. *Earth and Planetary Science Letters*, 415, 1–15. doi:
 965 10.1016/j.epsl.2015.01.016
- 966 Süß, M. P., & Shaw, J. H. (2003). Pwave seismic velocity structure derived from
 967 sonic logs and industry reflection data in the Los Angeles basin, California. *Jour-*
 968 *nal of Geophysical Research: Solid Earth*, 108(B3). doi: 10.1029/2001jb001628
- 969 Taborda, R., Azizzadeh-Roodpish, S., Khoshnevis, N., & Cheng, K. (2016, June).
 970 Evaluation of the southern California seismic velocity models through simulation
 971 of recorded events. *Geophysical Journal International*, 205(3), 1342–1364. doi:
 972 10.1093/gji/ggw085
- 973 Tape, C., Liu, Q., Maggi, A., & Tromp, J. (2009, August). Adjoint Tomography of
 974 the Southern California Crust. *Science*, 325(5943), 988–992. doi: 10.1126/science
 975 .1175298
- 976 Tsai, V. C., & Atiganyanun, S. (2014, October). Green’s Functions for Surface
 977 Waves in a Generic Velocity Structure. *Bulletin of the Seismological Society of*
 978 *America*, 104(5), 2573–2578. doi: 10.1785/0120140121
- 979 Tso, C.-H. M., Iglesias, M., Wilkinson, P., Kuras, O., Chambers, J., & Binley, A.
 980 (2021, February). Efficient multiscale imaging of subsurface resistivity with un-
 981 certainty quantification using ensemble Kalman inversion. *Geophysical Journal*
 982 *International*, 225(2), 887–905. doi: 10.1093/gji/ggab013
- 983 USGS. (2020). *U.S. Geological Survey and California Geological Survey, Quater-*
 984 *nary fault and fold database for the United States*, [https://www.usgs.gov/natural-](https://www.usgs.gov/natural-hazards/earthquake-hazards/faults)
 985 *hazards/earthquake-hazards/faults*, Accessed April 12, 2021. USGS.
- 986 Valentine, A. P., & Sambridge, M. (2020a, March). Gaussian process models—I. A
 987 framework for probabilistic continuous inverse theory. *Geophysical Journal Inter-*
 988 *national*, 220(3), 1632–1647. doi: 10.1093/gji/ggz520
- 989 Valentine, A. P., & Sambridge, M. (2020b, March). Gaussian process models—II.
 990 Lessons for discrete inversion. *Geophysical Journal International*, 220(3), 1648–
 991 1656. doi: 10.1093/gji/ggz521
- 992 Wright, T. L. (1991). Structural Geology and Tectonic Evolution of the Los Angeles
 993 Basin, California. In *Active Margin Basins* (pp. 35–134). American Association of
 994 Petroleum Geologists: AAPG Special Volumes.
- 995 Yerkes, R. F., Campbell, R. H., Alvarez, R. M., & Bovard, K. R. (2005). Prelimi-
 996 nary geologic map of the Los Angeles 30’ × 60’ Quadrangle, southern California.
 997 *US Geological Survey Open File Report*, 1019, 1559–1573.